Experimental and Theoretical Studies of Hyperthermal N + O₂ Collisions

Adriana Caracciolo,[a] Juan Carlos San Vicente Veliz,[b] Dandan Lu,[c] Hua Guo,[c,*] Markus Meuwly,[b,*] and Timothy K. Minton[a,*]

[a] *Ann and H.J. Smead Department of Aerospace Engineering Sciences, University of Colorado Boulder, CO 80303, USA*

[b] *Department of Chemistry, University of Basel, CH-4056 Basel, Switzerland*

[c] *Department of Chemistry and Chemical Biology, University of New Mexico, Albuquerque, New Mexico 87131, USA*

*: corresponding authors: hguo@unm.edu; m.meuwly@unibas.ch; tminton@colorado.edu

Abstract

      The dynamics of hyperthermal $N(^4S) + O_2$ collisions were investigated both experimentally and theoretically. Crossed molecular beams experiments were performed at an average center-of-mass (c.m.) collision energy of $\langle E_{coll} \rangle = 77.5$ kcal mol^{-1}, with velocity- and angle-resolved product detection by a rotatable mass spectrometer detector. Non-reactive ($N + O_2$) and reactive ($NO + O$) product channels were identified. In the c.m. reference frame, the non-reactively scattered N atoms and reactively-scattered NO molecules were both directed into the forward direction with respect to the initial direction of the reagent N atoms. On average, more than 90% of the available energy ($\langle E_{avl} \rangle = 77.5$ kcal mol^{-1}) was retained in translation of the non-reactive products ($N + O_2$), whereas a much smaller fraction of the available energy for the reactive pathway ($\langle E_{avl} \rangle = 109.5$ kcal mol^{-1}) went into translation of the NO + O products, and the distribution of translational energies for this channel was broad, indicating extensive internal excitation in the nascent NO molecules. The experimentally derived c.m. translational energy and angular distributions of the reactive products suggested at least two dynamical pathways to the formation of NO + O. Quasiclassical trajectory (QCT) calculations were performed with a collision energy of $E_{coll} = 77$ kcal mol^{-1} using two sets of potential energy surfaces, denoted as PES-I and PES-II, and these theoretical results were compared to each other and to the experimental results. PES-I is a reproducing kernel Hilbert space (RKHS) representation of multi-reference configurational interaction (MRCI) energies, while PES-II is a many-body permutation invariant polynomial (MB-PIP) fit of complete active space second order perturbation (CASPT2) points. The theoretical investigations were both consistent with the experimental suggestion of two dynamical pathways to produce NO + O, where reactive collisions may proceed on the doublet ($1^2A'$) and quartet ($1^4A'$) surfaces. When analyzed with this theoretical insight, the experimental c.m. translational energy and angular distributions were in

2

reasonably good agreement with those predicted by the QCT calculations, although minor differences were observed which are discussed. Theoretical translational energy and angular distributions for the non-reactive $N + O_2$ products matched the experimental translational energy and angular distributions almost quantitatively. Finally, relative yields for the non-reactive and reactive scattering channels were determined from the experiment and from both theoretical methods, and all results are in reasonable agreement.
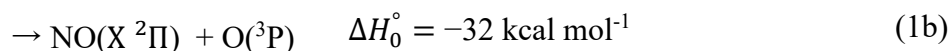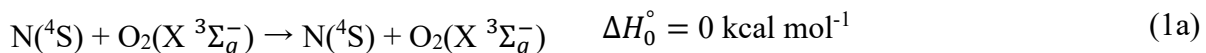
I. INTRODUCTION

Hypersonic flight through Earth's atmosphere generates a thin, high-temperature, shock layer that surrounds the vehicle surface.[1] Within this shock layer, the gas is often in a state of strong thermochemical nonequilibrium.[2] The internal energy of the gas (rotational and vibrational) quickly increases and ultimately leads to dissociation of molecular species into atomic species. Dissociation of molecular nitrogen and oxygen produces N and O atoms, which can in turn collide with undissociated O_2 and N_2 and lead to nitric oxide formation.[3, 4] These reactions are commonly referred to as Zeldovich reactions:[5]

$$N + O_2 \rightarrow NO + O \tag{1}$$

$$O + N_2 \rightarrow NO + N \tag{2}$$

With its relative ease of reaction and importance in combustion, numerous investigations of N + O_2 reaction kinetics have been conducted. These investigations focused mainly on rate constants[6-11] and NO vibrational distribution measurements.[12-14] Among the kinetic studies, Clyne and Thrush[7] determined the rates for Reaction (1) with temperatures between T = 412 and 755 K, which can be derived by the expression $k = 8.3 \times 10^{12} e^{(-\frac{7100}{RT})}$ cm^3 mol^{-1} s^{-1}. Wilson extended the measurements to a wider range of temperatures (T = 300 and 910 K)[8] by monitoring the disappearance of N atoms generated in a microwave discharge in a fast-flow system.[9] Wilson's results ($k = 1.41 \pm 0.07 \times 10^{13} e^{(-\frac{7900 \pm 200}{RT})}$ cm^3 mol^{-1} s^{-1}) were in good agreement with the previous kinetics studies.[6, 10, 11] For the NO vibrational distribution measurements, Caledonia et al. studied the fundamental and overtone band emissions of NO(X$^2\Pi$) generated in hyperthermal collisions of N atoms with O_2 molecules.[14] The authors observed highly vibrationally excited NO products (v = 0-7) and derived the relative vibrational state-specific cross sections, which were found to be in good agreement with previous theoretical predictions.[15] Laser induced fluorescence

4

measurements by Herm *et al.* showed that 22% of the available energy is channeled into NO vibration ($v \geq 2$).[12] On the other hand, Winkler et al. estimated that 34% of the reaction exothermicity goes into NO product vibration.[13] These experimental studies have been complemented by theoretical investigations. Potential energy surfaces (PESs) for Reaction (1) have been reported by several authors.[16-26] Overall, rate coefficients calculated from these PESs are in reasonably good agreement with experiment.[17, 19, 20, 27-32] Predictions of the NO product vibrational state distributions have also been reported,[17, 19, 27, 31, 33-35] and the PESs have also been used to investigate non-reactive scattering between N and O_2.[25] Finally, PESs have been constructed for understanding the photochemistry of NO_2.[36, 37]

Although these extensive previous studies provided a detailed characterization of the N + O_2 system, both existing theoretical and experimental investigations lack information about non-reactive and reactive collisions of N + O_2 under the extreme conditions in hypersonic shock layers, where collision energies may be tens of kcal mol^{-1}. Caracciolo et al. have recently reported an experimental study on the reverse of Reaction (1) at a collision energy of $\langle E_{coll} \rangle = 84.0$ kcal mol^{-1},[38] and subsequent theoretical calculations by Lu et al. have reasonably reproduced most of the measurements.[39] In addition, theoretical studies of the NO + O reaction have been reported by Castro-Palacio et al.[24, 32] In the present paper, a joint experimental and theoretical investigation involving all three of these groups on the dynamics of hyperthermal N + O_2 collisions is reported. We focus our attention on products generated from non-reactive (1a) and reactive collisions (1b):

$$N(^4S) + O_2(X\,^3\Sigma_g^-) \rightarrow N(^4S) + O_2(X\,^3\Sigma_g^-) \qquad \Delta H_0^\circ = 0 \text{ kcal mol}^{-1} \qquad (1a)$$

$$\rightarrow NO(X\,^2\Pi) + O(^3P) \qquad \Delta H_0^\circ = -32 \text{ kcal mol}^{-1} \qquad (1b)$$

5

The reaction enthalpies reported in Reaction (1b) were determined at $T = 0$ K from the formation enthalpies of the products and reactants.[40] We probed these processes experimentally by conducting crossed molecular beams scattering experiments at an average collision energy of $\langle E_{coll} \rangle = 77.5$ kcal mol^{-1} (for experimental details see Section II). Angular and velocity distributions for both the non-reactive and reactive scattering pathways were collected in the experimentally accessible laboratory angular range for the N and NO products. Scattering measurements of Reaction (1b) suggested that the N + O$_2$ reaction may proceed via two different dynamical pathways. These two pathways were modeled as reactions on the doublet and quartet PESs of the NO$_2$ system.

The N(^{4}S) + O$_2$(X $^3\Sigma_g^-$) asymptote is correlated with one doublet, one quartet, and one sextet, while the NO(X $^2\Pi$) + O(^{3}P) asymptote is correlated with six doublet and six quartet states. The two asymptotes are connected adiabatically with the lowest doublet (1^2A′) and quartet (1^4A′) states, as shown in Figure 1. The ground electronic state is the doublet, with a deep well featuring the stable NO$_2$ species having C_{2v} symmetry. These states within a spin manifold can potentially be coupled to higher electronic states through derivative couplings, and the states in different spin manifolds can also couple via spin-orbit couplings; nevertheless, to first order it is reasonable to assume that adiabatic dynamics will dominate. Based on this assumption, the overall reactivity can be approximated by a multiplicity-weighted reactivity on the two (doublet and quartet) spin states.

For the lowest doublet and quartet states, there are several *ab initio* PESs, but we used the recently constructed PESs by San Vicente et al. (denoted as PES-I)[25] and by Varga et al. (denoted as PES-II).[26] The former are reproducing kernel Hilbert space (RKHS)[41, 42] representations of multi-reference configurational interaction (MRCI) energies, while the latter are many-body permutation invariant polynomial (MB-PIP) fits of complete active space second order

6

perturbation (CASPT2) points. It is important to note that both sets of PESs were designed for hyperthermal collisions, as high-energy points are included in the *ab initio* data. In the work reported here, these two sets of PESs have been used to study the dynamics of Reactions (1a) and (1b) using quasi-classical trajectory (QCT) methods. We have compared the collision dynamics predicted by the two sets of PESs with the results of a crossed molecular beams scattering experiment. In so doing, we have gained a general understanding of hyperthermal $N + O_2$ collision dynamics and both the accuracy and consistency of the two theoretical methods used to describe these dynamics.

II. EXPERIMENTAL METHODS

The experiments were performed with a crossed molecular beams apparatus equipped with a hyperthermal atomic nitrogen beam source and a rotatable mass spectrometer detector.[43-49] A hyperthermal pulsed beam, containing N atoms and N_2 molecules, was generated with a CO_2 TEA laser detonation source (~ 7 J pulse^{-1}) with a repetition rate of 2 Hz, employing molecular nitrogen as the precursor gas at a pressure of 500 psig and a piezoelectric pulsed valve of our own design. The corresponding hyperthermal beam contained N and N_2 in a mole ratio of 0.35:0.65, respectively, with a nominal velocity of 8 km s^{-1}. The velocity distribution was large ($\sim$6-9 km s^{-1}), so a synchronized 17.8 cm diameter chopper wheel, with three equally spaced 1.5 mm wide slots operating at 400 Hz, was used to select a narrow portion of the overall beam pulse. Figure 2a shows the resulting velocity distribution after the chopper wheel, with its maximum at 8077 m s^{-1} and a full width half-maximum (FWHM) of $\sim$690 m s^{-1}. The hyperthermal N/N_2 beam was crossed at 90° with a pulsed supersonic beam of molecular oxygen (O_2) with a velocity of 960 m s^{-1}. The O_2 beam was generated with a piezoelectric pulsed valve having a nozzle diameter of 1.0 mm and

7

a stagnation pressure of 2400 Torr. The velocity used for the O_2 beam was not measured directly; this value was found to be the most consistent with the average velocities of inelastically scattered N atoms colliding with O_2 with an average N-atom velocity of 8095 m s^{-1}. The average collision energy of this distribution is $<E_{coll}> = 77.5$ kcal mol^{-1} and its overall distribution is shown in Figure 2b.

The scattered products were ionized by a Brink-type electron-impact (EI) ionizer[50] positioned 33.7 cm from the nominal crossing points of the two beams, in the innermost region of the triply differentially pumped rotatable mass spectrometer detector. Scattered products that entered the detector were ionized, and then the ions were mass selected by a quadrupole mass spectrometer and registered with a Daly ion detector.[51] The registered ion counts, which are proportional to number density of products that entered the ionizer, were accumulated with the use of a multichannel scaler. Number density distributions of scattered products, $N(t)$, typically called time-of-flight (TOF) distributions, were acquired as a function of their flight time from the crossing region of the two beams to the ionizer. These TOF distributions were collected over a range of laboratory angles from $\Theta = 6°$ to $51°$, where the laboratory angle, Θ, is defined as the detection direction with respect to the hyperthermal N-atom beam ($\Theta = 0°$). Figure 3 shows the nominal Newton diagram for N + O_2 collisions under our experimental conditions for non-reactive (blue) and reactive (red) channels within the laboratory angular detection range used in this experiment (shaded yellow area), assuming that all the available energy, $\langle E_{avl} \rangle$, is channeled into product translation. The available energy for each channel can be derived as follows:

$$\langle E_{avl} \rangle = \langle E_{coll} \rangle - \Delta H_0^{\circ} \tag{2}$$

Based on Eq. (2), the available energy for products originating from non-reactive collisions will be equal to the average collision energy ($\langle E_{avl} \rangle = 77.5$ kcal mol^{-1}), while for the reactive

https://doi.org/10.26434/chemrxiv-2023-cf93b ORCID: https://orcid.org/0000-0003-4577-7879 Content not peer-reviewed by ChemRxiv. License: CC BY-NC-ND 4.0

channel $\langle E_{avl} \rangle$ is higher by 32 kcal mol^{-1}, the exothermicity of Reaction (1b). The $N(t)$ distributions collected at each laboratory angle were integrated to obtain the laboratory angular distributions, $N(\Theta)$. Individual TOF distributions were collected for 200 molecular beam pulses at $m/z = 14$ (^{14}N$^+$) and 28 (^{14}N$_2^+$) and for 1000 pulses at $m/z = 30$ (^{14}N^{16}O$^+$). These distributions were collected in 2° and 3° increments for $6° \leq \Theta \leq 12°$ and $12° \leq \Theta \leq 51°$ laboratory ranges, respectively. The increase in angular increment reduced the data accumulation time for the range of detection angles where the signal was not changing as rapidly. TOF distributions for relevant m/z ratios were collected by first increasing Θ from 6° to 51° and then decreasing Θ from 51° to 6°, constituting one cycle of data collection. The overall data acquisition consisted of one cycle of increasing and decreasing Θ for non-reactively scattered N and N$_2$ products and three cycles for reactively scattered NO products. The individual TOF distributions registered for each product and at each Θ were added together. The raw TOF distributions for N were corrected for the dissociative ionization of N$_2$ to produce N$^+$. To apply this correction, the TOF distributions for $m/z = 14$ and 28 were collected with a pure N$_2$ beam. The integrated TOF distribution collected for $m/z = 14$ was found to be 12% of the integrated TOF distribution for $m/z = 28$ under these experimental conditions; thus, for a given Θ, the TOF distribution collected at $m/z = 28$ was multiplied by 0.12 and the result was subtracted from the TOF distribution collected at $m/z = 14$. This correction was applied to the TOF distributions for N-atom products at $m/z = 14$, which contained a component from dissociative ionization of N$_2$ that came from inelastic collisions of N$_2$ with O$_2$ as a result of N$_2$ in the hyperthermal N/N$_2$ beam.

III. THEORETICAL METHODS

A. Potential Energy Surfaces

As mentioned in Section I, our focus is on the adiabatic dynamics involving the $1^2A'$ and $1^4A'$ states. There are two sets of PESs that were used in our QCT calculations, both containing adiabatic PESs for these two states.

PES-I[25] was developed using the reproducing kernel Hilbert space (RKHS) method[41, 42] to represent a total of ~10,000 (~7000 for the NO + O and ~3000 for the N + O_2 channel) energies at the MRCI+Q (Davidson correction) level of theory. The grid in both the reactant and product channels was defined in Jacobi coordinates (r, R, θ), where the R-grid included 28 points between 1.4 and 12.0 a_0, the distance r was covered by 20 points between 1.5 and 4.0 a_0, and the angular grid contained 13 angles from a Gauss-Legendre quadrature (169.796°, 156.577°, 143.281°, 129.967°, 116.647°, 103.324°, 90.100°, 76.676°, 63.353°, 50.033°, 36.719°, 23.423°, 10.204°). Further details about the *ab initio* calculation and PES construction can be found in Ref. [25]. These PESs have previously been used to study the forward and reverse rates of Reaction (1b).[25]

PES-II[26] was based on about 8000 CASPT2 energy points, which were fit using a many-body (MB) method,[52] where the two-body parts are accurate diatomic potentials and the three-body part is expressed with connected permutation invariant polynomials (PIPs)[53] in mixed-exponential-Gaussian bond order variables (MEGs). Similar to PES-I, grids in both the reactant and product channels were used to generate the points for the fitting. The grids in the bond lengths covered the range of 3.40 – 9.45 a_0, with 30 points in the angular coordinate. These PESs have been used in a previous QCT study of hyperthermal NO + O collisions.[39]

10

B. Quasi-Classical Trajectory Calculations

The QCT calculations used in the present work have been extensively described in the literature,[54] so only the essential parameters are given. 500,000 trajectories were calculated on each PES with the O_2 reactant in its rovibrational ground state ($v = 0$, $j = 0$). The initial reactant separation was 8.0 Å, and a trajectory was terminated when the collision partners or the products were separated by 9.0 Å or more. If the separating atom was N, the collision was classified as "inelastic", whereas if the products were $NO_A + O_B$ or $NO_B + O_A$ the collision was classified as "reactive". For the former, all elastic trajectories with final product states ($v' = 0$, $j' = 0$) were removed. The impact parameter was chosen from a uniformly distributed random number $\zeta \in [0,1]$, according to $b = b_{max}\zeta^{1/2}$ with $b_{max} = 3.5$ Å, which was large enough to converge the inelastic and reactive cross sections.

For a given spin quantum number S, the integral cross section (ICS) for a particular channel (reactive or non-reactive, denoted by n) was determined as follows:

$$\sigma_n^{[S]} = \pi b_{max}^2(E_{coll})P_n^{[S]}(E_{coll}), \tag{2}$$

where the probability $P_n^{[S]}$ is given by the ratio:

$$P_n^{[S]} = \frac{N_n^{[S]}}{N_{total}^{[S]}}. \tag{3}$$

$N_n^{[S]}$ and $N_{total}^{[S]}$ are, respectively, the number of trajectories in channel n and the total number of trajectories. In the QCT simulations, a collision energy of $E_{coll} = 77$ kcal mol^{-1} was used, which is very close to the average experimental collision energy of $\langle E_{coll} \rangle = 77.5$ kcal mol^{-1} (see Figure 2).

The differential cross-section (DCS) was determined according to

$$\frac{d\sigma_n^{[S]}}{dW} = \frac{\sigma_n dP_n^{[S]}/d\theta}{2\pi\sin(\theta)}, \tag{4}$$

11

where $\sigma_n^{[S]}$ is the ICS at the collision energy and $dP_n^{[S]}/d\theta$ is the probability density for channel n, with scattering angle θ defined as

$$\theta = \cos^{-1}\left(\frac{\vec{v}_i \cdot \vec{v}_f}{|\vec{v}_i||\vec{v}_f|}\right), \tag{5}$$

where $\vec{v}$ denotes the relative velocity vector and the subscripts i and f denote initial and final states, respectively. We define $\vec{v}_i = \vec{v}_N - \vec{v}_{O_2}$ for both the inelastic and reactive channels. For reactive scattering, we define $\vec{v}_f = \vec{v}_{ON} - \vec{v}_O$; in this way, $\theta = 0°$ and $\theta = 180°$ correspond to forward and backward scattering, respectively, relative to the initial velocity of N atoms in the c.m. frame. To compute the total cross sections, we consider the statistical weights for each spin state, which are 1/3 and 2/3 for the doublet and quartet states, respectively.

More details of the QCT calculations, particularly the assignment of the product ro-vibrational quantum numbers, can be found in Supporting Information (SI).

IV. EXPERIMENTAL RESULTS

A. Data Analysis Approach

The measured TOF and angular distributions are number densities recorded in the laboratory frame, $N(t)$ and $N(\Theta)$, respectively. However, detailed information on the reaction dynamics derives from the scattered flux in the c.m reference frame. Microscopic information such as c.m. translational energy $P(E_T)$ and angular $T(\theta)$ distributions cannot be obtained directly by deconvoluting the experimentally measured distributions in the laboratory frame. Thus, a forward convolution approach[45, 55] has been employed to analyze the experimental data. This method starts with trial c.m. distributions and uses a Jacobian coordinate transformation that accounts for the incident beam distributions and other experimental effects to calculate the laboratory frame $N(t)$

and $N(\Theta)$ distributions, which are then compared with the measured distributions. The input $P(E_T)$ and $T(\theta)$ distributions are iteratively adjusted until the best fits of the experimental data are reached. The uncertainties of the best-fit c.m. distributions were estimated by varying the shapes of the input c.m. translational energy and angular distributions that yielded predicted $N(t)$ and $N(\Theta)$ distributions that were within the statistical noise of these distributions. Additional simulations of the experimental data were carried out by using input c.m. $P(E_T)$ and $T(\theta)$ distributions obtained from QCT calculations described in Section IIIB. Best-fit distributions obtained for the non-reactive and reactive channels are described in Sections IV.B and IV.C, while the c.m. distributions derived from QCT calculations are described and compared in Section V.

B. Non-Reactive Scattering

TOF distributions of N-atom products were measured in the laboratory frame to characterize the dynamics of non-reactive collisions of $N(^4S)$ with $O_2(X\,^3\Sigma_g^-)$. Conservation of energy and momentum dictates that the measurement of scattered N-atom velocity and angular distributions reveals the velocity and angular distributions of O_2 molecules scattered in the opposite direction from the N atoms (Figure 3). Given the range of laboratory angles probed in this experiment, detected N atoms must originate from high-impact-parameter, non-reactive collisions, which lead to forward scattering. Figure 4a shows three representative TOF distributions measured for $m/z = 14$ (N^+), while the laboratory angular distribution is shown in Figure 4b. The superimposed lines on the experimental data (yellow circles) in Figures 4a and 4b correspond to the curves which are the outcome of the best-fit center-of-mass translational energy $P(E_T)$ and angular $T(\theta)$ distributions, shown in Figures 4c and 4d, respectively. In this experiment, N-atom products were probed only in the range, $0° \leq \theta \leq 78°$. The angular range over which the

experiment is blind for N-atom detection ($79° \leq \theta \leq 180°$) is represented as the gray shaded area in Figure 4d. The c.m. angular distribution obtained for N atoms (Figure 4d) has a strong forward peak, with negligible probability for $\theta > 40°$. This behavior is reflected in the laboratory angular distribution (Figure 4b), where the integrated number density decreases rapidly with increasing Θ and reaches a nominal low value for $\Theta \geq 30°$. The average translational energy obtained from the $P(E_T)$ distribution in Figure 4c was found to be $\langle E_T \rangle = 73.3$ kcal mol^{-1}, which indicates that, on average, ~97% of the available energy ($\langle E_{avl} \rangle = 77.5$ kcal mol^{-1}) is transformed into product translation. Thus, non-reactive collisions leave very little rotational or vibrational excitation in the scattered O_2 molecules. Both the fraction of E_{avl} in translation and the width of the $P(E_T)$ distribution (FWHM ~ 3 kcal mol^{-1}) are comparable to those observed for the non-reactive scattering of O + NO.[38]

Figure S1a shows the c.m. velocity flux map associated with the non-reactive N-atom product, where the two arrows correspond to the velocity of the reactants in the c.m. frame, while the dashed circles represent the non-reactive scattering limit by assuming that all the available energy is transformed into translation of N + O_2 products.

C. Reactive Scattering

The dynamics of the reactive scattering channel, Reaction (1b), were characterized through the detection of the $^{14}N^{16}O$ product at $m/z = 30$. Representative TOF distributions acquired at this mass-to-charge ratio are shown in Figure 5a, and the laboratory angular distribution is depicted in Figure 5d. After significant effort at optimizing the fits to all the laboratory distributions for NO, we concluded that a minimum of two dynamical pathways to this product must exist, corresponding to two sets of c.m. translational energy and angular distributions. An example of

14

two sets of c.m. distributions that provided a good overall fit to the experimental data in Figure 5a,d is shown as the black curves in Figure 6. Justification for the conclusion of at least two dynamical pathways is presented in Figure S2, where the fits predicted from only one set of $P(E_T)$ and $T(\theta)$ distributions (Figure S3) are shown. It may be seen in Figure S2 that the predicted TOF distributions for the smaller laboratory angles of $\Theta = 8°\text{-}24°$ fit the observed distributions reasonably well. However, for $\Theta > 24°$, the maxima in the predicted TOF distributions shift to flight times that are faster than the corresponding maxima in the experimental TOF distributions. This shift also results in a less-than-satisfactory fit of the leading edges and tails of the TOF distributions at larger laboratory angles. All attempts to achieve fits to the data with one set of $P(E_T)$ and $T(\theta)$ distributions that were as good as the two-component fits shown in Figure 5 failed. Although the laboratory angular distributions could be fit well in both cases (Figures 5d and S2c), the constraints required to fit the TOF distributions well suggested that the NO products that scattered more forward in the c.m. frame must arise from a reaction pathway that channels more energy into translation than the pathway that results in NO products that scatter more uniformly over a broad angular range. The two sets of $P(E_T)$ and $T(\theta)$ distributions (Figure 6) that gave the best fits to the laboratory data reflect this observation. It should be noted, however, that satisfactory overall fits to the experimental TOF and angular distributions could be obtained with other sets of $P(E_T)$ and $T(\theta)$ distributions, and the only really meaningful constraint was that one set required a higher average translational anergy and more sharply forward-peaking angular distribution than the other set.

The conclusion of at least two dynamical pathways that lead to NO products may be interpreted with the aid of theory. As shown in Figure 1, there are two adiabatic pathways via the two PESs corresponding to the lowest doublet and quartet states of the system. Within this

15

assumption, the relative weights of the quartet and doublet channels should be 2/3 and 1/3, respectively. In our best-fit sets of $P(E_T)$ and $T(\theta)$ distributions, the set that naturally had the higher weight was interpreted as arising from the quartet (Q) pathway and the set with lower weight was interpreted as arising from the doublet (D) pathway. The best-fit distributions in Figure 5a are thus labeled as Q and D based on the assumed quartet and doublet components, respectively. In addition, the associated c.m. distributions in Figure 6 are labeled as quartet and doublet. In Figure 6c,d, the nominal c.m angular range where the NO products were probed is also shown ($0° \leq \theta \leq 90°$); thus, the extrapolations of the experimental $T(\theta)$ distributions beyond this range are not constrained by the experimental data. The experimental c.m. angular distributions depicted in Figure 6c,d (black curves) suggest that the NO products scatter mainly in the forward direction, with the products scattering on the quartet PESs showing a much stronger propensity for forward scattering than those scattering on the doublet PESs. The $T(\theta)$ distribution associated with the quartet contribution decreases to half of its initial value for $\theta = 45°$. On the other hand, the best-fit $T(\theta)$ distribution obtained for the doublet component slowly decreases and reaches half its initial value at $\theta = 90°$. The $P(E_T)$ distribution for the quartet component (Figure 6a) has an average translational energy of $\langle E_T \rangle = 70.6$ kcal mol^{-1}. This distribution is also broad, with a FWHM of approximately 61 kcal mol^{-1}). On the other hand, the $P(E_T)$ distribution for the doublet contribution (Figure 6b) is narrower by 9 kcal mol^{-1} (FWHM ~ 52 kcal mol^{-1}) with respect to the quartet $P(E_T)$ distribution, and the average translational energy determined for this distribution is $\langle E_T \rangle = 43.7$ kcal mol^{-1}. Thus, the average energy for the doublet $P(E_T)$ distribution is almost 27 kcal mol^{-1} lower than that for the quartet $P(E_T)$ distribution. When considering the weighted contributions of both the quartet and doublet components, the overall average fraction of the available energy that goes into translation

16

($\langle f_T \rangle = \langle E_T \rangle / \langle E_{avl} \rangle$) of the NO + O products is ~52%, which is close to the value $\langle f_T \rangle \sim 58\%$, that was found for the reverse reaction, $O + NO \rightarrow O_2 + N$.[38]

Figure 7 shows c.m. velocity flux maps associated with NO products that originated from reactive collisions, where the two arrows in each flux map correspond to the velocities of the reactants in the c.m. frame, and the radius of the dashed circle represents the maximum velocity of NO if all the available energy goes into translational energy of the NO + O products. Panels (a), (b), and (c) of Figure 7 are calculated, respectively, from the $P(E_T)$ and $T(\theta)$ distributions derived from PES-I, PES-II, and the experimental results (see Figure 6), where the $P(E_T)$ and $T(\theta)$ distributions are assumed to be uncoupled and the total flux as a function of translational energy and c.m. scattering angle may be represented as the product of two independent functions: $P(E_T,\theta)$ = $P(E_T)T(\theta)$.

D. Relative Product Yields

Relative product yields were obtained for the $N + O_2$ reaction from the integrated cross sections (ICSs), which are derived from the experimental differential cross sections (DCSs). The detailed procedure has been described previously elsewhere.[38-56] The ICSs were weighted by the electron-impact ionization cross-sections for the relevant products, which were taken from the literature.[57-59] To estimate the relative yields, the transmission of the quadrupole mass filter was assumed to be constant in the explored range of mass-to-charge ratios ($14 \leq m/z \leq 30$). From the best-fit analysis (Figures 4, 5a,d, and 6), the relative yields obtained for the non-reactive and reactive channels were determined to be 0.65 ± 0.14 and 0.35 ± 0.14, respectively. The relative yields of NO originating from the best-fit quartet and doublet pathways were 0.19 and 0.16, respectively. These latter two values were derived from the best-fit experimental results in Figure

17

6; the uncertainties in these values could not be determined because the data were not sufficiently resolved to constrain the two fits beyond the conclusion of at least two dynamical pathways. Note that the relative yields are correlated (as are the associated uncertainties). Based on the increase of the detection sensitivity with the ion mass, the relative yield obtained for the non-reactive channel can be considered as lower limit, which, in turn, implies that the value obtained for the reactive channel is an upper limit.

V. THEORETICAL RESULTS AND COMPARISON WITH EXPERIMENT

An important question in this work is whether the two sets of PESs used in the QCT calculations yield comparable dynamical results. Given that these two sets of PESs are based on different *ab initio* methods and representations, some differences are expected. In Figure 8, contour plots of the two sets of PESs for the doublet and quartet states are shown for the reactive channel. The PESs are expressed as a function of the N-O and O-O distances with the angle between the N-O and O-O vectors optimized for every combination of separations. Although there are some differences between them, the overall topographies of the PESs are similar. Both doublet and quartet PESs suggest a direct abstraction mechanism with small entrance channel barriers for this exothermic reaction. There is no significant well in either the doublet or quartet abstraction pathway. In Figure 9, contour plots of the same PESs are displayed for the insertion channel, in which the PESs along the C_{2v} approach by N into O_2 are plotted. These contours are reported with respect to the N-O_2 (R) and O-O (r) distances. It is clear that the insertion pathways for both doublet and quartet surfaces have high barriers. There is a deep well on the ground $1^2A'$ state PES for the NO_2 species, which is clearly visible. The insertion barriers are 65.9 (69.2) and 55.1 (52.0) kcal mol^{-1} for the doublet and quartet, respectively, on PES-I (PES-II). At E_{coll} = 77 kcal mol^{-1}, the

18

insertion pathway is viable for both states, but the lower barrier of the quartet obviously makes it more likely. As the dynamics at high collision energies can be significantly influenced by the repulsive part of the PES in the short range, the cuts of the PESs in both $N + O_2$ and $O + NO$ collisions are also compared in Figure 10, with diatomic distances fixed at their respective asymptote and Jacobi angles.

Table I reports the calculated fractions of the inelastic and reactive $N + O_2$ collisions on the doublet and quartet PESs, along with a comparison of the calculated weighted average branching fractions for inelastic and reactive scattering to the experimental branching fractions for non-reactive and reactive collisions. The agreement for calculations using the two PESs is good, and both are consistent with the experimental results. The experiment suggests that about 35% of the collisions lead to reaction, and the theoretical results predict a reactive fraction closer to 25-30%. The contributions from the two spin states can be determined separately from theoretical simulations, and they are also quite similar to each other, regardless of the spin quantum number. It should be noted that the contribution from elastic scattering depends on the chosen maximum impact parameter used in the QCT calculations. On the other hand, the experimental fraction for the non-reactive channel includes both elastic and inelastic scattering. Hence, the experimental fraction for the inelastic scattering would be even smaller, which suggests that the theoretical values may be too large. However, the experimental uncertainties do not allow this conclusion to be asserted with high confidence.

Without considering the spin multiplicity, the calculated absolute ICSs on the doublet and quartet states are 7.39 and 6.77 $Å^2$ on PES-I and 8.72 and 6.81 $Å^2$ on the PES-II, respectively. Both calculations suggest that the reactivity is comparable in the two spin channels. However, the quartet contribution to the total ICS is larger because of its larger statistical weight of 2/3.

19

https://doi.org/10.26434/chemrxiv-2023-cf93b **ORCID:** https://orcid.org/0000-0003-4577-7879 Content not peer-reviewed by ChemRxiv. **License:** CC BY-NC-ND 4.0

The experimental and theoretical c.m. translational energy and angular distributions for the non-reactive channel, Reaction (1a), are compared in Figure S5, where the c.m. angular distributions (Figure S5c,d) pertain to the N-atom product. The calculated c.m. angular distributions (Figure S5c,d) are quite similar and do not differ significantly from the experimental angular distribution (Figure S5c,d, black curves). On the other hand, the c.m. translational energy distributions for scattering on PES-II (Figure S5a,b, red curves) have qualitatively lower average energies than those for scattering on PES-I (Figure S5a,b, green curves), which agrees well with the experimental translational energy distribution (Figure S5a,b, black curves). Figure S6 shows that the laboratory TOF and angular distributions are predicted fairly well by the $P(E_T)$ and $T(\theta)$ distributions calculated by both PESs, but the lower predicted c.m. translational energy from PES-II is reflected in the slight shift in the calculated TOF distributions to longer flight times as compared to the experimental TOF distributions (Figure S6b). Figure S6c,d shows that both PESs capture the forward bias in the N-atom laboratory angular distributions equally well, which is also evident in the c.m. velocity-flux maps in Figure S1.

The experimental and theoretical translational energy and angular distributions for the reactive channel, Reaction (1b), are compared in Figure 6, where the c.m. angular distributions (Figure 6c,d) pertain to the NO product. For the $P(E_T)$ distributions (Figure 6a,b), the agreement between the calculations on PES-I and PES-II is better for the dominant quartet channel, and both are in general agreement with the experimental results. For the minor doublet channel, the agreement is less satisfactory, as the distribution calculated on PES-II overestimates the low energy region, while the calculated distribution on PES-I is in much better agreement with the experimental result. Referring to the angular distributions of NO (Figures 6c,d), both the PES-I and PES-II calculations for dominant quartet channel predict more sideways scattering than the

20

experiment, which is dominated by forward scattering. For the minor doublet channel, the agreement between the two calculations and their agreement with the slight forward bias of the experimental fit is reasonable, although quantitative differences are evident.

Figure 5 compares the best-fit curves for the laboratory TOF (panel (a)) and angular (panel (d)) distributions for NO products and the simulations of the experimental data derived by forward convolution from the theoretical $P(E_T)$ and $T(\theta)$ distributions shown in Figure 6. As mentioned in Section IV.C, the red and green curves depicted in Figures 5b,c,e,f were obtained by weighting the quartet and the doublet distributions based on their degeneracies. By comparing calculated TOF distributions of NO with the experimental distributions (Figures 5b,c), it can be seen that the calculated curves show a tail or even an additional peak at longer times which is not present in the experimental TOF distributions. This discrepancy originates from the theoretical c.m. translational energy and angular distributions (Figure 6), which go through a forward-convolution procedure to determine the predicted laboratory distributions. The $P(E_T)$ distributions derived for the doublet PES-I and PES-II do not go to zero near $E_T = 0$ kcal mol^{-1} (Figure 6b), which leads to an enhancement of the slow tails in the TOF distributions. Furthermore, the $T(\theta)$ distribution obtained from PES-II exhibits a sideways bias, with its maximum value corresponding to the c.m. angle in the laboratory frame, Θ_{cm}, which accentuates the slow TOF signal in the laboratory frame. Thus, the effect on the slow tail is more noticeable for the prediction of PES-II than that of PES-I, because the $T(\theta)$ distribution from PES-II has a maximum precisely at the angle that corresponds to Θ_{cm}, whereas the maximum in the $T(\theta)$ distribution from PES-II corresponds to a smaller Θ and therefore higher velocities in the laboratory frame (i.e., shorter times in the TOF distribution). The net result is that, while both sets of c.m. distributions from PES-I and PES-II capture the general

21

shapes of the experimental TOF and angular distributions of NO products, the discrepancy in the slow tail of the TOF distributions remains unresolved.

The QCT results have also been converted to c.m. velocity-flux maps for NO products, and the results are presented in Figures 7d,e. The calculated velocity-flux maps are derived from the weighted average of the two spin channels, as described in Section III, and they come from the fully correlated c.m. velocity and angular distributions, $P(v,\theta)$, rather than from the product function, $P(E_T)T(\theta)$, from which the velocity-flux maps in Figures 7a,b,c were derived. The QCT velocity-flux maps from both PES-I (Figure 7d) and PES-II (Figure 7e) feature a dominant forward scattering peak for NO, as is seen in the experimental result (Figure 7a), but that from PES-II also shows pronounced backward scattering, which is not seen in the result from PES-I (note that the experiment is not sensitive to backward scattering of NO). The overall theory-experiment agreement is reasonable, although there are significant deviations. The overall performance of PES-I seems to be slightly better than that of PES-II.

As expected, the NO product has significant internal excitation, which is reflected in the $P(E_T)$ distributions for the reactive channel, Reaction (1b), where it was found experimentally that the overall average fraction of the available energy that goes into translation of the NO + O products is ~52%. The vibrational distributions of the NO products from $N + O_2$ reactions on both the doublet and quartet PESs, as well as the sum weighted by the spin multiplicities, are shown in Figure 11a,b,c (left panels), where the vibrational populations are obtained by summing over the rotational populations. Both, PES-I and PES-II yield qualitatively similar distributions, featuring monotonically decreasing probabilities with increasing vibrational quantum number. The quartet state yields a cooler vibrational distribution than the doublet state. We have examined the impact of zero-point energy violation in the product state distribution using the hard ZPE criterion,[60]

22

namely excluding ZPE-violating trajectories in the product channel. The resulting distributions, shown in Figure S7, indicate that their impact is minimal for this exoergic reaction.

In the right panels of Figure 11, the NO rotational state distributions, summed over the vibrational state populations, are shown. PES-I and PES-II yield significant rotational excitation, with populations all the way to the highest accessible rotational state of NO ($j \sim 152$) at this energy. However, there are significant quantitative differences between the rotational state distributions obtained from the quartet and doublet channels. The more pronounced differences are for the rotational distributions which are considerably more structured for PES-I than for PES-II. On the other hand, the envelopes of the rotational distributions agree quite closely. This difference in the rotational distributions may be due to a more pronounced angular anisotropy of PES-I compared with PES-II.

To gain insight into the reaction mechanism, Figure 12 reports the correlation between the impact parameter and the scattering angle. On both sets of PESs, the reactive channel is dominated by a direct abstraction mechanism, as evidenced by the pronounced inverse correlation of the scattering angle with the impact parameter. In particular, small impact parameters lead to backward rebound scattering whereas large impact parameters result in forward (stripping) scattering. The prevalent direct mechanism is consistent with the PESs shown in Figure 8. In addition to the main abstraction mechanism, there is also evidence for a minor contribution resulting from insertion. There is clearly an outlier region in Figure 12 for $b \in (0.5, 1.0)$ Å, in which the scattering is exclusively forward biased. Analysis of the trajectories indicate that the reaction proceeds via insertion of N into O_2, followed by breaking of one NO bond, as shown in Figure S8. The insertion pathway is shown in Figure 9, and the experimental collision energy is above the barriers in both the quartet and doublet channels. Since the insertion barrier in the quartet channel is lower than

that of doublet, the insertion channel for the quartet seems to be more prominent. Overall, however, this channel constitutes only about 5% of the total probability.

VI. DISCUSSION

To reproduce hyperthermal collisions quantitatively, theoretical simulations require accurate PESs in a much larger configurational and energy space than those required for room temperature collisions. The results presented in Sections II and III indicate that the two sets of PESs yield qualitatively similar results, and both are in reasonable, but not perfect, agreement with the experimental results. The consistency in the theoretical calculations is important as the two sets of PESs were constructed using different *ab initio* methods and representation strategies. The qualitatively similar results using the same dynamics method gives us confidence in the predictive power of such calculations. On the other hand, it is equally apparent that there are many quantitative differences between the results obtained from simulations using these two sets of PESs, including product translational energy and angular distributions, as well as branching fractions. Such differences are most likely the result of the different *ab initio* and representation methods in constructing these PESs. In addition, there are several quantitative discrepancies between theory and experiment, which are much larger than those commonly seen in low energy dynamics studies. They could be attributed to several factors, including the neglected non-adiabatic coupling and involvement of excited electronic states, intrinsic errors in the *ab initio* calculations, and lack of points in certain regions of configurational space that are relevant to hyperthermal collisions. In addition, the experimental analysis procedure also contains significant uncertainties, as has been discussed.

24

A key deficiency of the current theoretical models is the neglect of non-adiabatic coupling with higher electronic states. As shown in Figure 1, the experimental collision energy allows access to several low-lying excited channels. If the $O(^1D)$ + NO(X) and $O(^1S)$ + NO(X) product channels were involved, we would expect peaks with onsets at 66.3 and 15.2 kcal mol^{-1}. Although we do not see obvious additional peaks in the experimental translational energy distribution, the current detection scheme is probably not sensitive enough to identify these excited channels if their branching fractions are comparatively low. As a result, the question about the participation of excited channels remains unresolved. In the theoretical approach, a multistate dynamics calculation would require the accurate determination of the diabatic potential energy matrix (DPEM) involving all the relevant states. Although significant progress has been made recently,[61, 62] it is still extremely challenging to construct such DPEMs, particularly at the high energy where many electronic states are present. These states can be coupled via either derivative coupling within a spin manifold or spin-orbit coupling between different spin manifolds, which further complicate the calculations.

The two *ab initio* calculations used to generate the PESs were performed using well-established multi-reference methods, which have comparable performance. Both representation methods are also known to be robust. Indeed, the comparison of the PESs in Figures 8-10 shows similar behaviors.

As discussed extensively in Sec. II, there is significant uncertainty in the fitting of the experimental TOF and angular distributions. First, there is the assumption that the $P(E_T)$ and $T(\theta)$ distributions are factorizable, although this simplification is somewhat mitigated by the two components used in the fitting. More importantly, the weighting of the two components is not unique, and a wide range of relative weightings yields overall fits that are within the uncertainties

25

in the data. The ultimate solution to this problem is to perform velocity map imaging (VMI) experiments, which provide the global representation of the differential cross section with product state resolution. This can be done with REMPI detection of NO or O, and future experiments are planned to obtain higher-fidelity data for comparison with the theoretical calculations.

VII. CONCLUSIONS

In this work, we report a joint experiment-theory investigation of hyperthermal collisions of N and O_2. The crossed molecular beams experiment was performed with an average collision energy of $\langle E_{coll} \rangle = 77.5$ kcal mol^{-1}. Both non-reactive and reactive channels were detected. The non-reactive channel is dominated by a narrow, forward-scattered angular distribution and very little loss of translational energy, while the exoergic reactive channel to produce NO + O features a broad translational energy distribution with a forward bias. Based on the translational energy distribution, the NO product is expected to have significant internal excitation, but the quantum state distribution was not measured.

These experimental observations are semi-quantitatively reproduced by QCT calculations on two sets of independently developed PESs. These calculations were performed on the lowest doublet and quartet adiabatic PESs, with the assumption that the non-adiabatic coupling to excited electronic states is small/negligible. This assumption seems to be reasonable, judging from the overall agreement with experimentally determined c.m. translational energy and angular distributions based on this two-state model. However, quantitative differences do exist and their possible origins are discussed. Future refinements of this model by including excited electronic states and their coupling are probably needed to improve the agreement.

26

Theoretical calculations indicated that the quartet state provides the main contribution of the reactivity, as a result of its larger weighting factor, which is proportional to the spin multiplicity. The reaction mainly follows a direct mechanism, featuring straightforward abstraction of O from the O_2 reactant by N, although a minor insertion pathway has also been identified.

The validation of the relevant PESs in this work opens the door to accurate calculations of the reaction rates under hyperthermal conditions, which is underway in our groups. The reliable high-temperature rate coefficients will lower the uncertainty in the modeling of hypersonic shock layers. In addition, the PESs also offer a platform for understanding energy transfer between the translational and internal modes of NO, which is dictated by the inelastic scattering channel.

■ ASSOCIATED CONTENT

Supporting Information:

The Supporting Information is attached to this manuscript/

■ AUTHOR INFORMATION

Corresponding Authors:

Timothy K. Minton – *Ann and H.J. Smead Department of Aerospace Engineering Sciences, University of Colorado Boulder, Boulder, CO 80303, United States*; orcid.org/0000-0003-4577-7879; Email: tminton@colorado.edu

Hua Guo – *Department of Chemistry and Chemical Biology, University of New Mexico, Albuquerque, New Mexico 87131, United States;* orcid.org/0000-0001-9901-053X; Email: hguo@unm.edu

Markus Meuwly – *Department of Chemistry, University of Basel, CH-4056 Basel, Switzerland;* orcid.org/0000-0001-7930-8806; Email: m.meuwly@unibas.ch

Authors:

Adriana Caracciolo – *Ann and H.J. Smead Department of Aerospace Engineering Sciences, University of Colorado Boulder, Boulder, 80303, United States;* orcid.org/0000-0002-2588-7627; Email: adriana.caracciolo@colorado.edu

Dandan Lu – *Department of Chemistry and Chemical Biology, University of New Mexico, Albuquerque, New Mexico 87131, United States;* Email: ddlu@unm.edu

Juan Carlos San Vicente Veliz – *Department of Chemistry, University of Basel, CH-4056 Basel, Switzerland;* orcid.org/0000-0002-5939-0571; Email: j.sanvicente@unibas.ch

Notes:

The authors declare no competing financial interest.

Table I. Branching fractions of the inelastic and reactive $N + O_2$ collisions at $E_{coll} = 77$ kcal/mol, assuming NO is initially in its ground rovibrational state.

	Inelastic scattering	Reactive scattering
Doublet, PES-I	0.783	0.192
Quartet, PES-I	0.802	0.176
Weighted average, PES-I	0.796	0.181
Doublet, PES-II	0.725	0.275
Quartet, PES-II	0.776	0.224
Weighted average, PES-II	0.759	0.241
Experiment	0.65±0.14 [a]	0.35±0.14

[a] The experiment was conducted with $\langle E_{coll} \rangle = 77.5$ kcal mol^{-1}, and the branching fraction for "Inelastic Scattering" includes both the inelastic and elastic channels (i.e., all non-reactive scattering).

References:

(1) Leyva, I. The relentless pursuit of hypersonic flight. *Phys. Today* **2017**, *70*, 30-36.

(2) Colonna, G.; Bonelli, F.; Pascazio, G. Impact of fundamental molecular kinetics on macroscopic properties of high-enthalpy flows: The case of hypersonic atmospheric entry. *Phys. Rev. Fluids* **2019**, *4*, 033404.

(3) Brooks, S. B.; Lewis, M. J.; Dickerson, R. R. Nitric oxide emissions from the high-temperature viscous boundary layers of hypersonic aircraft within the stratosphere. *J. Geophys Res. Atmos.* **1993**, *98*, 16755-16760.

(4) Litvintsev, A. S.; Molchanova, A. N.; Bondar, Y. A. NO production on the reentry spececraft thermal protection system surface in the direct simulation Monte Carlo method. *Phys.: Conf. Ser.* **2019**, *1404*, 012118.

(5) Zeldovich, Y. The oxidation of nitrogen in combustion explosions. *Acta Physicochemica USSR* **1946**, *21*, 577-628.

(6) Kistiakowsky, G. B.; Volpi, G. G. Reactions of nitrogen atoms. I. Oxygen and oxides of nitrogen. *J. Chem. Phys.* **1957**, *27*, 1141-1149.

(7) Clyne, M. A. A.; Thrush, B. A.; Norrish, R. G. W. Kinetics of the reactions of active nitrogen with oxygen and with nitric oxide. *Proc. Royal Soc. A* **1961**, *261*, 259-273.

(8) Wilson, W. E. Rate constant for the reaction $N + O_2 \rightarrow NO + O$. *J. Chem. Phys.* **1967**, *46*, 2017-2018.

(9) Westenberg, A. A.; de Haas, N. Atom-molecule kinetics at high temperature Using ESR detection. Technique and results for $O + H_2$, $O + CH_4$, and $O + C_2H_6$. *J. Chem. Phys.* **1967**, *46*, 490-501.

(10) Becker, K. H.; Groth, W.; Kley, D. The Rate Constant of the Aeronomic Reaction $N + O_2$. *Z. Naturforsch. A* **1969**, *24*, 1280-1281.

(11) Baulch, D. L.; Cobos, C. J.; Cox, R. A.; Frank, P.; Hayman, G.; Just, T.; Kerr, J. A.; Murrells, T.; Pilling, M. J.; Troe, J.; Walker, R. W.; Warnatz, J. Evaluated kinetic data for combustion modelling, Supplement I. *J. Phys. Chem. Ref. Data* **1994**, *23*, 847.

(12) Herm, R. R.; Sullivan, B. J.; Whitson, M. E. Nitric oxide vibrational excitation from the $N(^4S) + O_2$ reaction. *J. Chem. Phys.* **1983**, *79*, 2221-2230.

(13) Winkler, I.; Stachnik, R. A.; Steinfeld, J. I.; Miller, S. M. Determination of NO (v=0–7) product distribution from the $N(^4S) + O_2$ reaction using two-photon ionization. *J. Chem. Phys.* **1986**, *85*, 890-899.

(14) Caledonia, G. E.; Krech, R. H.; Oakes, D. B.; Lipson, S. J.; Blumberg, W. A. M. Products of the reaction of 8 km/s $N(^4S)$ and O_2. *J. Geophys Res. Atmos.* **2000**, *105*, 12833-12837.

(15) Sharma, R. D.; Dothe, H.; Duff, J. W. Model of the 5.3 μm radiance from NO during the sunlit terrestrial thermosphere. *J. Geophys Res.* **1998**, *103*, 14753-14768.

(16) Walch, S. P.; Jaffe, R. L. Calculated potential surfaces for the reactions: $O + N_2 \rightarrow NO + N$ and $N + O_2 \rightarrow NO + O$. *J. Chem. Phys.* **1987**, *86*, 6946-6956.

(17) Braunstein, M.; Duff, J. W. Theoretical study of the $N(^2D) + O_2(X\,^3\Sigma_g^-) \rightarrow O + NO$ reaction. *J. Chem. Phys.* **2000**, *113*, 7406-7413.

(18) Sayós, R.; Oliva, C.; González, M. The lowest doublet and quartet potential energy surfaces involved in the $N(^4S) + O_2$ reaction. I. Ab initio study of the C_s-symmetry $(^2A', ^4A')$ abstraction and insertion mechanisms. *J. Chem. Phys.* **2001**, *115*, 1287-1297.

(19) González, M.; Miquel, I.; Sayós, R. Ab initio, variational transition state theory and quasiclassical trajectory study on the lowest $^2A'$ potential energy surface involved in the $N(^2D) + O_2(X\,^3\Sigma_g^-) \rightarrow O(^3P) + NO(X\,^2\Pi)$ atmospheric reaction. *J. Chem. Phys.* **2001**, *115*, 2530-2539.

(20) Sayós, R.; Oliva, C.; González, M. New analytical $(^2A', ^4A')$ surfaces and theoretical rate constants for the $N(^4S) + O_2$ reaction. *J. Chem. Phys.* **2002**, *117*, 670-679.

(21) González, M.; Oliva, C.; Sayós, R. The lowest doublet and quartet potential energy surfaces involved in the N(^{4}S)+O$_2$ reaction. II. Ab initio study of the C$_{2v}$-symmetry insertion mechanism. *J. Chem. Phys.* **2002**, *117*, 680-692.

(22) Varandas, A. J. C. A realistic multi-sheeted potential energy surface for NO$_2$(^{2}A′) from the double many-body expansion method and a novel multiple energy-switching scheme. *J. Chem. Phys.* **2003**, *119*, 2596-2613.

(23) Mota, V. C.; Caridade, P. J. S. B.; Varandas, A. J. C. Ab initio-based global double many-body expansion potential energy surface for the first ^{2}A″ electronic state of NO$_2$. *J. Phys. Chem. A* **2012**, *116*, 3023-3034.

(24) Castro-Palacio, J. C.; Nagy, T.; Bemish, R. J.; Meuwly, M. Computational study of collisions between O(^{3}P) and NO(^{2}Π) at temperatures relevant to the hypersonic flight regime. *J. Chem. Phys.* **2014**, *141*, 164319.

(25) San Vicente Veliz, J. C.; Koner, D.; Schwilk, M.; Bemish, R. J.; Meuwly, M. The N(^{4}S) + O$_2$(X^{3}Σ–g) ↔ O(^{3}P) + NO(X^{2}Π) reaction: thermal and vibrational relaxation rates for the ^{2}A′, ^{4}A′ and ^{2}A′′ states. *Phys. Chem. Chem. Phys.* **2020**, *22*, 3927-3939.

(26) Varga, Z.; Liu, Y.; Li, J.; Paukku, Y.; Guo, H.; Truhlar, D. G. Potential energy surfaces for high-energy N + O$_2$ collisions. *J. Chem. Phys.* **2021**, *154*, 084304.

(27) Duff, J. W.; Bien, F.; Paulsen, D. E. Classical dynamics of the N(^{4}S) + O$_2$ (X^{3}Σ$_g^-$) ⟶ NO(X^{2}Π) + O(^{3}P) reaction. *Geophys. Res. Lett.* **1994**, *21*, 2043-2046.

(28) Valli, S. G.; Orrú, R.; Clementi, E.; Laganà, A.; Crocchianti, S. Rate coefficients for the N+O$_2$ reaction computed on an ab initio potential energy surface. *J. Chem. Phys.* **1995**, *102*, 2825-2832.

(29) Bose, D.; Candler, G. V. Thermal rate constants of the N$_2$+O→NO+N reaction using ab initio 3A″ and 3A′ potential energy surfaces. *J. Chem. Phys.* **1996**, *104*, 2825-2833.

(30) Balakrishnan, N.; Dalgarno, A. Rate coefficients for NO formation in energetic N+O$_2$ collisions. *Chem. Phys. Lett.* **1999**, *302*, 485-488.

(31) Defazio, P.; Petrongolo, C.; Oliva, C.; González, M.; Sayós, R. Quantum dynamics of the N(^{4}S)+O$_2$ reaction on the X^{2}A′ and a ^{4}A′ surfaces: Reaction probabilities, cross sections, rate constants, and product distributions. *J. Chem. Phys.* **2002**, *117*, 3647-3655.

(32) Castro-Palacio, J. C.; Bemish, R. J.; Meuwly, M. Communication: Equilibrium rate coefficients from atomistic simulations: The O(^{3}P) + NO(^{2}Π) ⟶ O$_2$(X^{3}Σ$_g^-$) + N(4S) reaction at temperatures relevant to the hypersonic flight regime. *J. Chem. Phys.* **2015**, *142*, 091104.

(33) Ramachandran, B.; Balakrishnan, N.; Dalgarno, A. Vibrational–rotational distributions of NO formed from N+O$_2$ reactive collisions. *Chem. Phys. Lett.* **2000**, *332*, 562-568.

(34) Caridade, P. J. B. S.; Varandas, A. J. C. Dynamics study of the N(^{4}S) + O$_2$ reaction and its reverse. *J. Phys. Chem. A* **2004**, *108*, 3556-3564.

(35) Sultanov, R. A.; Balakrishnan, N. Quantum mechanical investigations of the N(^{4}S)+O$_2$(X^{3}Σ$_g^-$)⟶ NO(X^{2}Π)+O(^{3}P) reaction. *J. Chem. Phys.* **2006**, *124*, 124321.

(36) Kurkal, V.; Fleurat-Lessard, P.; Schinke, R. NO$_2$: Global potential energy surfaces of the ground (1 ^{2}A$_1$) and the first excited (1 ^{2}B$_2$) electronic states. *J. Chem. Phys.* **2003**, *119*, 1489-1501.

(37) Ndengué, S.; Quintas-Sánchez, E.; Dawes, R.; Osborn, D. The low-lying electronic states of NO$_2$: Potential energy and dipole surfaces, bound states, and electronic absorption spectrum. *J. Phys. Chem. A* **2021**, *125*, 5519-5533.

(38) Caracciolo, A.; Zhang, J.; Lahankar, S. A.; Minton, T. K. Dynamics of inelastic and reactive collisions of ^{16}O(^{3}P) with ^{15}N^{18}O. *J. Phys. Chem. A* **2022**, *126*, 2091–2102.

(39) Lu, D.; Truhlar, D. G.; Guo, H. Reactive and nonreactive collisions between NO(X^{2}Π) and O(^{3}P) under hyperthermal conditions. *J. Phys. Chem. A* **2022**, *126*, 4277-4285.

(40) Chase, M. NIST-JANAF Thermochemical Tables, 4th Edition. *J. Phys. Chem. Ref. Data, Monograph 9* **1998**, 1-1951.

(41) Ho, T.-S.; Rabitz, H. A general method for constructing multidimensional molecular potentials energy surfaces from ab initio calculations. *J. Chem. Phys.* **1996**, *104*, 2584-2597.

(42) Unke, O. T.; Meuwly, M. Toolkit for the construction of reproducing kernel-based representations of data: Application to multidimensional potential energy surfaces. *J. Chem. Info. Model.* **2017**, *57*, 1923-1931.

(43) Garton, D. J.; Minton, T. K.; Maiti, B.; Troya, D.; Schatz, G. C. A crossed molecular beams study of the O(^{3}P)+H$_2$ reaction: Comparison of excitation function with accurate quantum reactive scattering calculations. *J. Chem. Phys.* **2003**, *118*, 1585-1588.

(44) Troya, D.; Schatz, G. C.; Garton, D. J.; Brunsvold, A. L. Crossed beamns and theoretical studies of the O(^{3}P) + CH$_4$ --> H + OCH$_3$ reaction excitation function. *J. Chem. Phys.* **2004**, *120*, 731-739.

(45) Garton, D., J.; Brunsvold, A., L.; Minton, T., K.; Troya, D.; Maiti, B.; Schatz, G., C. Experimental and theoretical investigations of the inelastic and reactive scattering dynamics of O(^{3}P) + D$_2$. *J. Phys. Chem. A* **2006**, *110*, 1327-1341.

(46) Brunsvold, A. L.; Zhang, J.; Upadhyaya, H. P.; Minton, T. K.; Camden, J. P.; Paci, J. T.; Schatz, G. C. Crossed-beams and theoretical studies of the O(^{3}P) + H$_2$O $\rightarrow$ HO$_2$ + H reaction excitation function. *J. Phys. Chem. A* **2007**, *111*, 10907-10913.

(47) Brunsvold, A. L.; Upadhyaya, H. P.; Zhang, J.; Cooper, R.; Minton, T. K.; Braunstein, M.; Duff, J. W. Dynamics of hyperthermal collisions of O(^{3}P) with CO. *J. Phys. Chem. A* **2008**, *112*, 2192-2205.

(48) Garton, D. J.; Minton, T. K.; Hu, W.; Schatz, G. C. Experimental and Theoretical Investigations of the Inelastic and Reactive Scattering Dynamics of O(3P) Collisions with Ethane. *J. Phys. Chem. A* **2009**, *113*, 4722-4738.

(49) Zhang, J.; Brunsvold, A. L.; Upadhyaya, H. P.; Minton, T. K.; Camden, J. P.; Garashchuk, S.; Schatz, G. C. Crossed-Beams and Theoretical Studies of Hyperthermal Reactions of O(3P) with HCl. *J. Phys. Chem. A* **2010**, *114*, 4905-4916.

(50) Brink, G. O. Electron bombardment molecular beam detector. *Rev. Sci. Instrum.* **1966**, *37*, 857-860.

(51) Daly, N. R. Scintillation-type mass spectrometer ion detector. *Rev. Sci. Instrum.* **1960**, *31*, 264-267.

(52) Murrell, J. N.; Carter, S.; Farantos, S. C.; Huxley, P.; Varandas, A. J. C. *Molecular Potential Energy Functions*; Wiley, 1984.

(53) Braams, B. J.; Bowman, J. M. Permutationally invariant potential energy surfaces in high dimensionality. *Int. Rev. Phys. Chem.* **2009**, *28*, 577–606.

(54) Truhlar, D. G.; Muckerman, J. T. Reactive scattering cross sections III: Quasiclassical and semiclassical methods. In *Atom-Molecule Collision Theory*, Bernstein, R. B. Ed.; Plenum, 1979; pp 505-566.

(55) Lee, Y. T. Reactive Scattering I: Nonoptical Methods. In *Atomic and Molecular Beam Methods*, Scoles, G. Ed.; Vol. 1; Oxford University Press:, 1988; pp pp 553-568.

(56) Pan, H.; Liu, K.; Caracciolo, A.; Casavecchia, P. Crossed beam polyatomic reaction dynamics: recent advances and new insights. *Chem. Soc. Rev.* **2017**, *46*, 7517-7547.

(57) Märk, T. D. Cross section for single and double ionization of N$_2$ and O$_2$ molecules by electron impact from threshold up to 170 eV. *J. Chem. Phys.* **1975**, *63*, 3731-3736.

(58) Stein, S. E. Infrared Spectra. In NIST Chemistry WebBook; RN 108-88-3; http://webbook.nist.gov (accessed on Aug 13, 2012). In *NIST Standard Reference Database Number 69*, Linstrom, P., Mallard, W. G. Eds.; National Institute of Standards and Technology:, 2005.

(59) Song, M.-Y.; Yoon, J.-S.; Cho, H.; Karwasz, G. P.; Kokoouline, V.; Nakamura, Y.; Tennyson, J. Cross Sections for Electron Collisions with NO, N$_2$O, and NO$_2$. *J. Phys. Chem. Ref. Data* **2019**, *48*, 043104.

(60) Guo, Y.; Thompson, D. L.; Sewell, T. D. Analysis of the zero‐point energy problem in classical trajectory simulations. *J. Chem. Phys.* **1996**, *104*, 576-582.

(61) Guan, Y.; Xie, C.; Yarkony, D. R.; Guo, H. High-fidelity first principles nonadiabaticity: Diabatization, analytic representation of global diabatic potential energy matrices, and quantum dynamics. *Phys. Chem. Chem. Phys.* **2021**, *23*, 24962-24983.

(62) Westermayr, J.; Marquetand, P. Machine learning for electronically excited states of molecules. *Chem. Rev.* **2021**, *121*, 9873-9926.
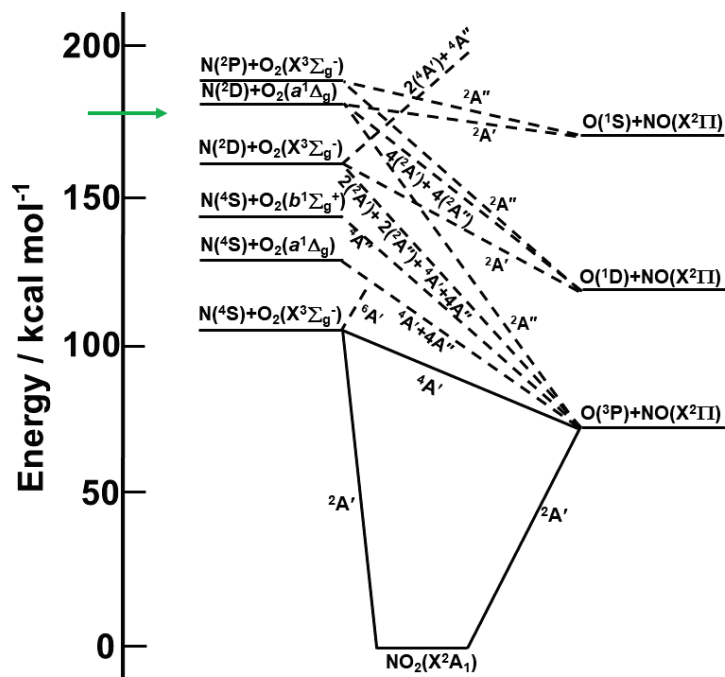
Figure 1. Correlation diagram for the N + O$_2$ → NO + O reaction. The green arrow marks the experimental collision energy. The solid lines represent the two adiabatic states included in the current calculations, while the dashed lines indicate excited electronic states not considered in the current study.
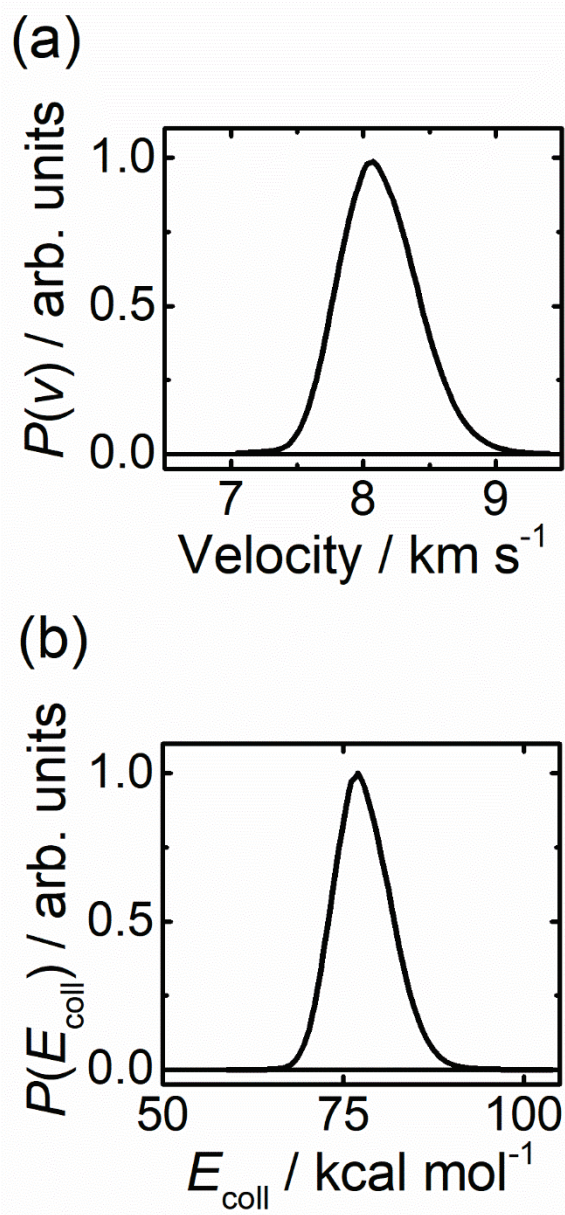
Figure 2. (a) Velocity distribution of the O-atom component in the O/O$_2$ hyperthermal beam (v_{peak} = 8077 m s^{-1}). (b) Center-of-mass collision energy distribution for N(^{4}S) collisions with O$_2$, determined by using a single velocity of the molecular oxygen beam of 960 m s^{-1}. The average collision energy of the distribution in (b) is $\langle E_{coll} \rangle$ = 77.5 kcal mol^{-1}.
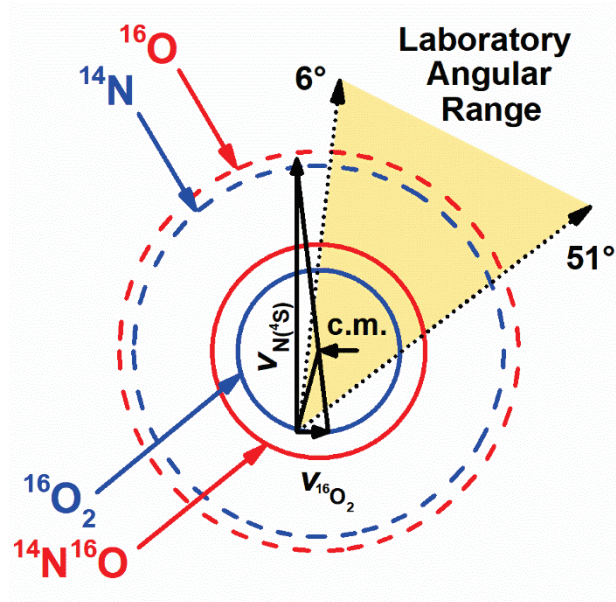
Figure 3. Newton diagram for N + O$_2$ collisions (E_{coll} = 77.5 kcal mol^{-1}). The radii of the circles represent the velocities of the non-reactive (^{14}N and ^{16}O$_2$) and reactive products (^{16}O and ^{14}N^{16}O) in the center-of-mass frame by assuming that all the available energy is channeled into product translational energy. The yellow shaded area represents the range of laboratory angles, Θ, explored in this experiment.
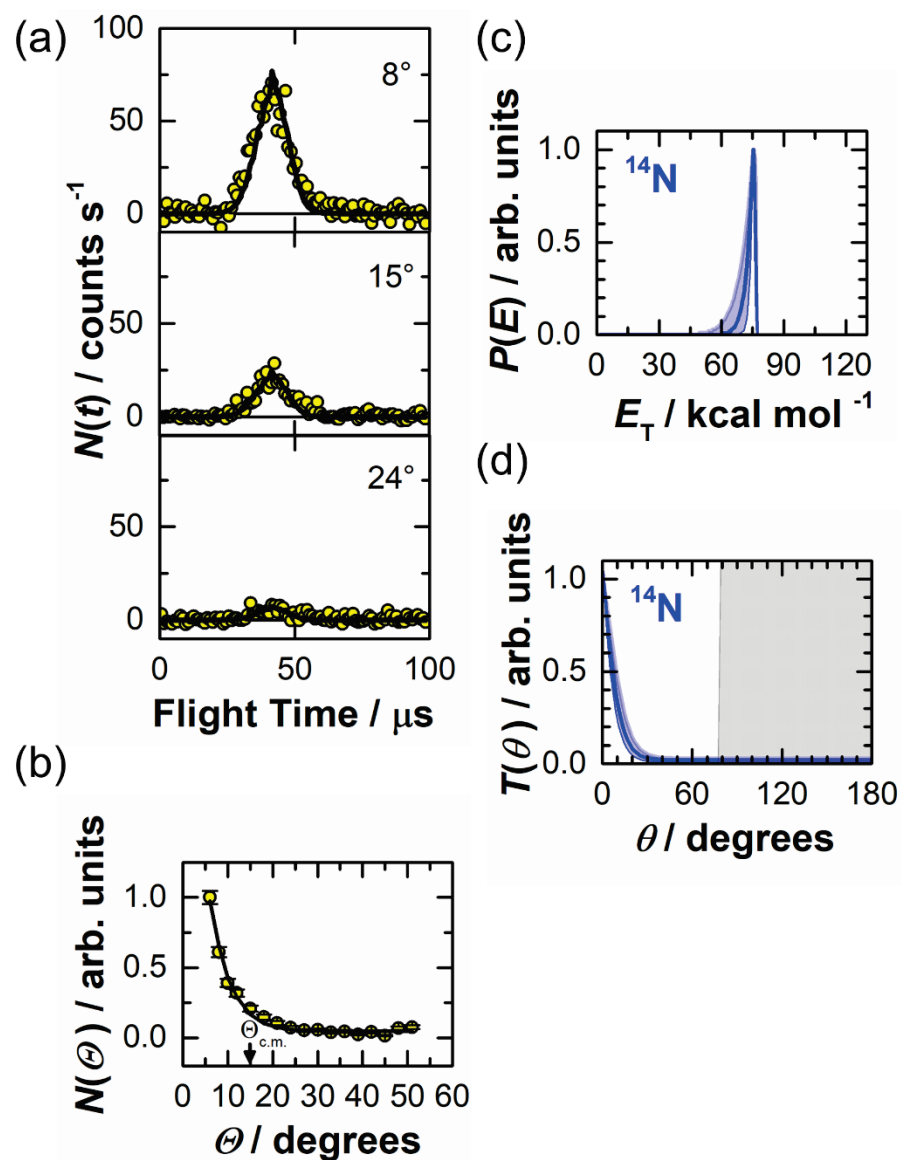
Figure 4. Representative TOF distributions (a) and relative angular distribution (b) observed for the non-reactively scattered N-atom products at $m/z = 14$ with $\langle E_{coll} \rangle = 77.5$ kcal mol^{-1}. The black solid lines superimposing the raw data (yellow circles) in (a) and (b) represent the best-fit curves, which are calculated from the forward convolution of the c.m. translational energy and angular distributions depicted in (c) and (d), respectively. The shaded blue areas shown in (c) and (d) correspond to 0.95 confidence limits, while the gray shaded regions indicate the detection limit for N-atom products in the c.m. angular range, where $\theta = 0°$ corresponds to the direction of the incident N atoms.
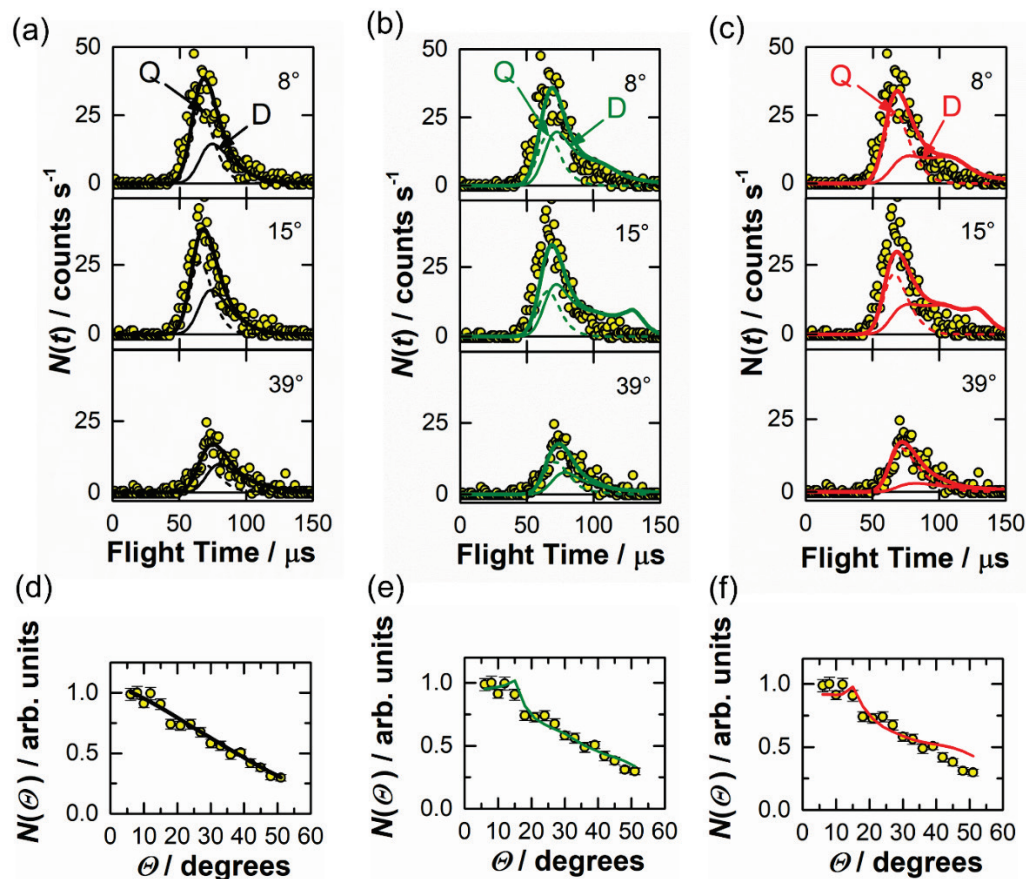
Figure 5. Representative TOF (a,b,c) and angular (d,e,f) distributions in the laboratory frame for the reactively scattered NO products at $m/z = 30$ with $\langle E_{avl} \rangle = 109.5$ kcal mol^{-1}. The black solid lines superimposing the raw data (yellow circles) in (a) and (d) represent the best-fit curves, which are calculated from the forward convolution of the c.m. translational energy and angular distributions depicted as black curves in Figure 6. The green solid lines superimposing the raw data (yellow circles) in (b) and (e) represent the QCT simulation curves that are calculated from the forward convolution of the c.m. translational energy and angular distributions from PES-I, depicted as green solid lines in Figure 6. The red solid lines superimposing the raw data (yellow circles) in (c) and (f) represent the QCT simulation curves that are calculated from the forward convolution of the c.m. translational energy and angular distributions from PES-II, depicted as green solid lines in Figure 6. In (a), (b), and (c) the single contributions from NO formed on the quartet (Q) and doublet (D) PESs are also shown.

38
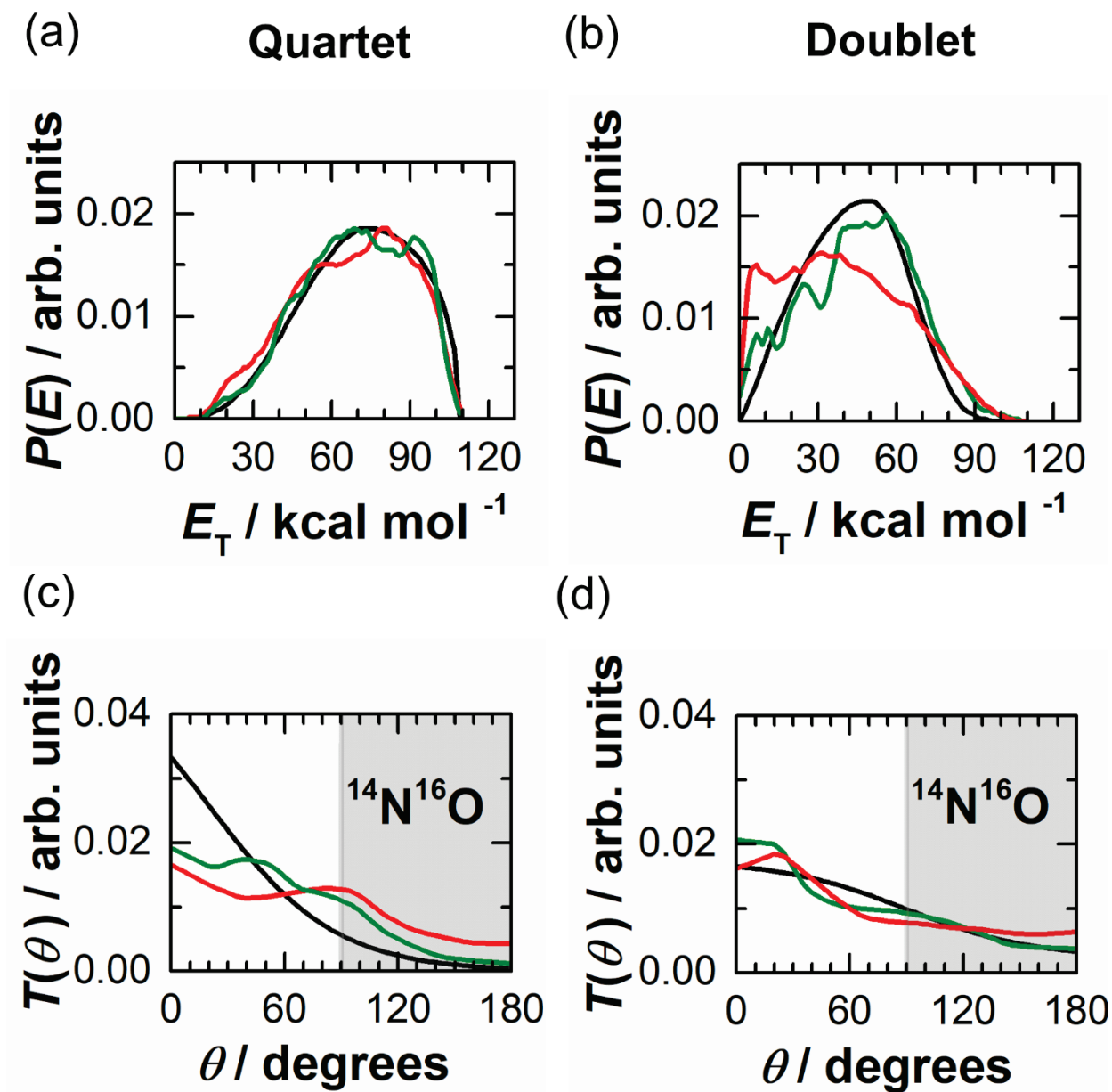
Figure 6. Optimized experimental c.m. translational energy (a,b) and angular (c,d) distributions (black curves) and corresponding QCT distributions from PES-I (green) and PES-II (red) for Reaction (1b) following the quartet (*lhs*) and doublet (*rhs*) surfaces. The angular distributions in (c) and (d) pertain to the NO product, where $\theta = 0°$ corresponds to the direction of the incident N atoms. The shaded gray regions in (c) and (d) represent the range of c.m. angles that were not probed in the experiment.

39
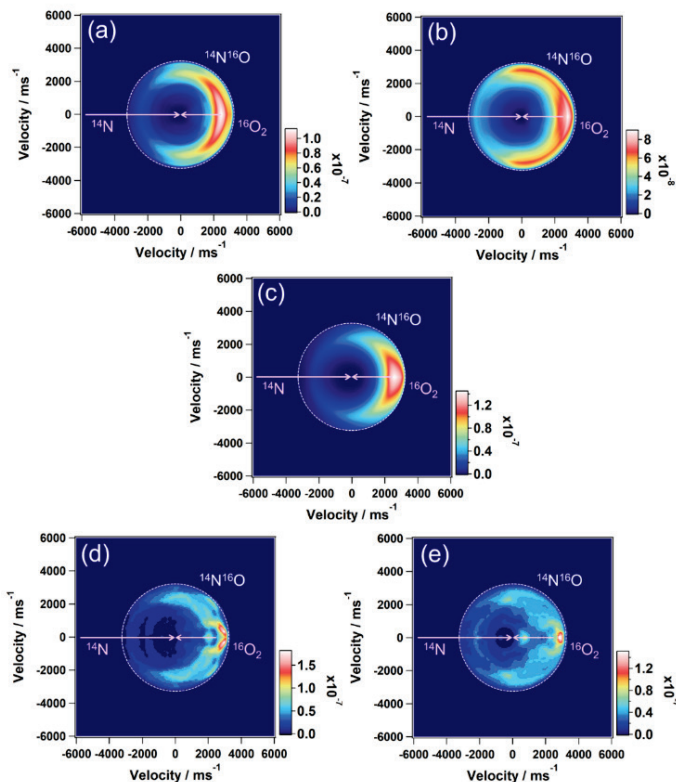
Figure 7. Center-of-mass velocity-flux maps for NO products of the N + O_2 reaction. (a), (b), and (c) were derived from the forward convolution method by using the c.m. translational energy and angular distributions derived from PES-I, PES-II, and the experiment, depicted in Figure 6 as green, red, and black curves, respectively. (d) and (e) are c.m. velocity-flux maps derived from PES-I and PES-II, respectively, without assuming that the $P(E_T)$ and $T(\theta)$ distributions are independent functions that can be factorized as $P(E_T)$ and $T(\theta)$, which has been assumed in (a), (b), and (c). In each panel, the arrows correspond to the initial velocity vectors of the reactants, and the radius of the dashed circle represents the maximum recoil velocity for the observed molecular product, given the constraints of energy and momentum conservation. The maximum flux for each c.m. velocity-flux map has been normalized to the associated area. The c.m. velocity-flux maps in (a), (b), (d), and (e) were obtained by weighting the c.m. functions according to the statistical spin weight for the quartet (2/3) and doublet states (1/3). The weighting for the c.m. velocity-flux map in (c) was the experimental best-fit weighting of 67% and 33% for the assumed quartet and doublet states, respectively.

40
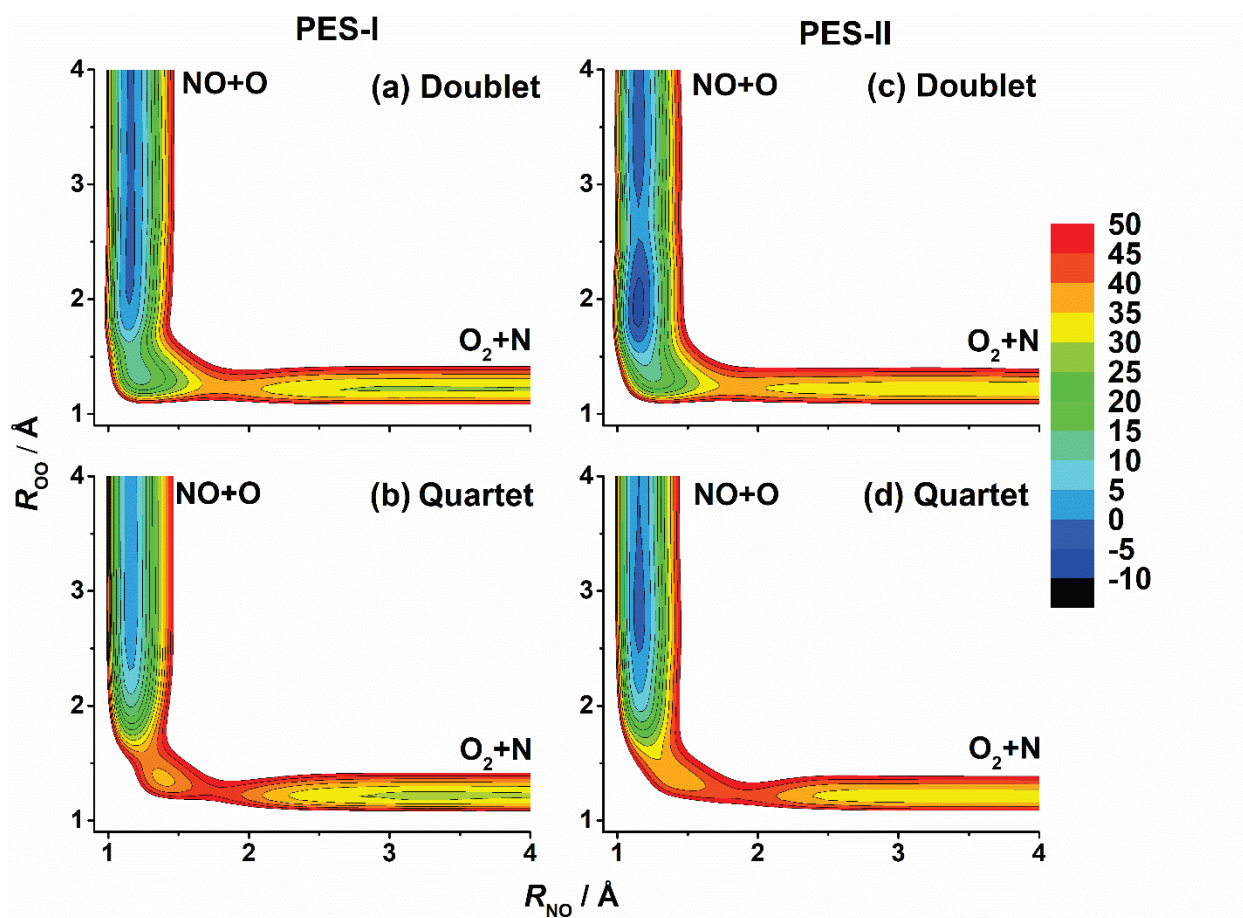
Figure 8. Contour plots of PES-I and PES-II for the $1^2A'$ and $1^4A'$ states as a function of the R_{NO} and R_{OO} distances, with the angle between the N-O and O-O vectors optimized along the N + OO approach. The energy is given in kcal mol^{-1} with the zero of energy defined at the NO + O asymptote.
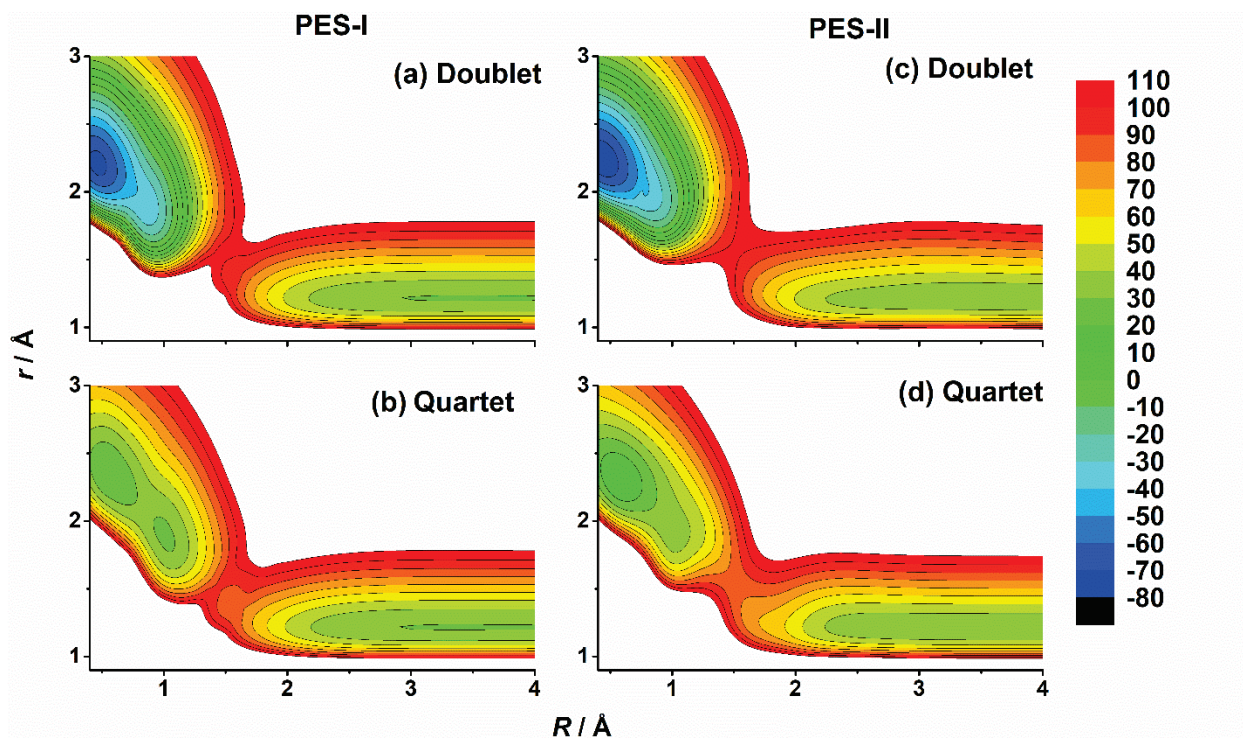
Figure 9. Contour plots of PES-I and PES-II for the $1^2A'$ and $1^4A'$ states as a function of r (the O-O distance) and R (the distance between N and the c.m. of O_2), with the Jacobi angle fixed at 90°. The energy is given in kcal mol^{-1} with zero defined as the NO + O asymptote.
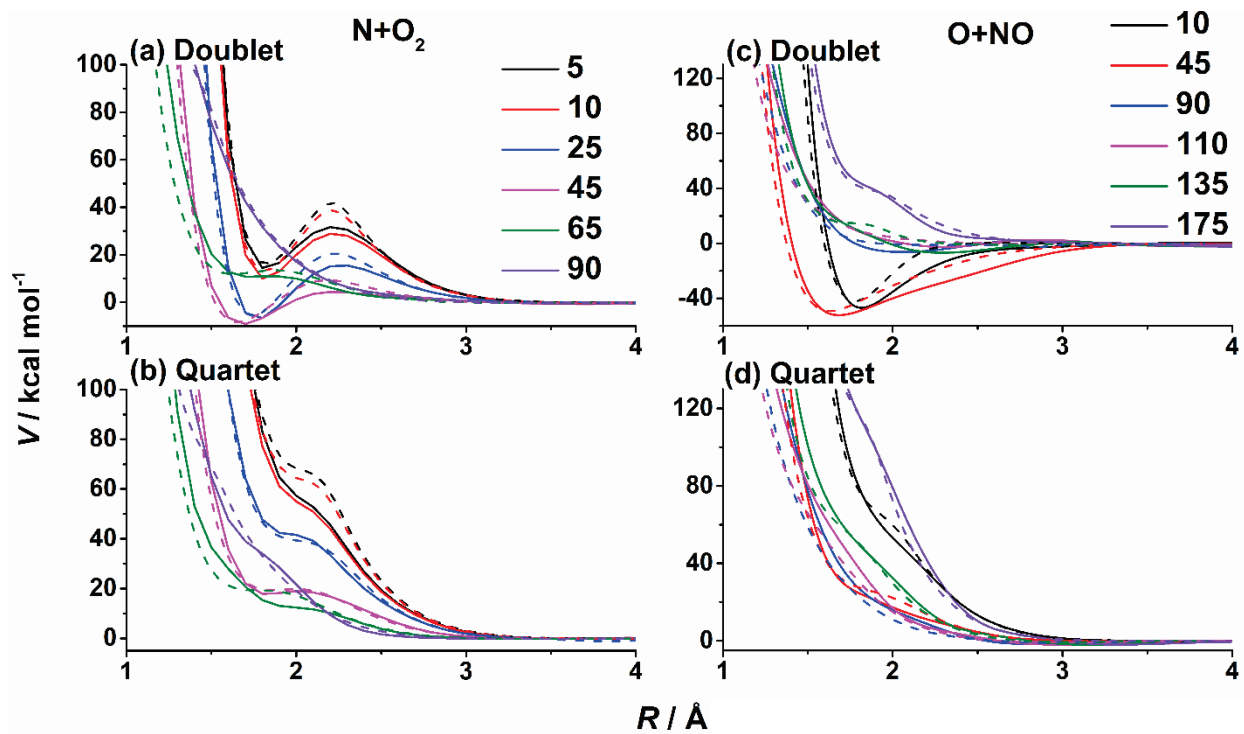
Figure 10. Cuts of PES-I (dashed lines) and PES-II (solid lines) for the $1^2A'$ and $1^4A'$ states in the $N + O_2$ (left panels) and $O + NO$ (right panels) Jacobi coordinates with the corresponding diatomic distances fixed at the asymptotic values. The energy is given in kcal mol^{-1} with zero defined in the respective asymptote.
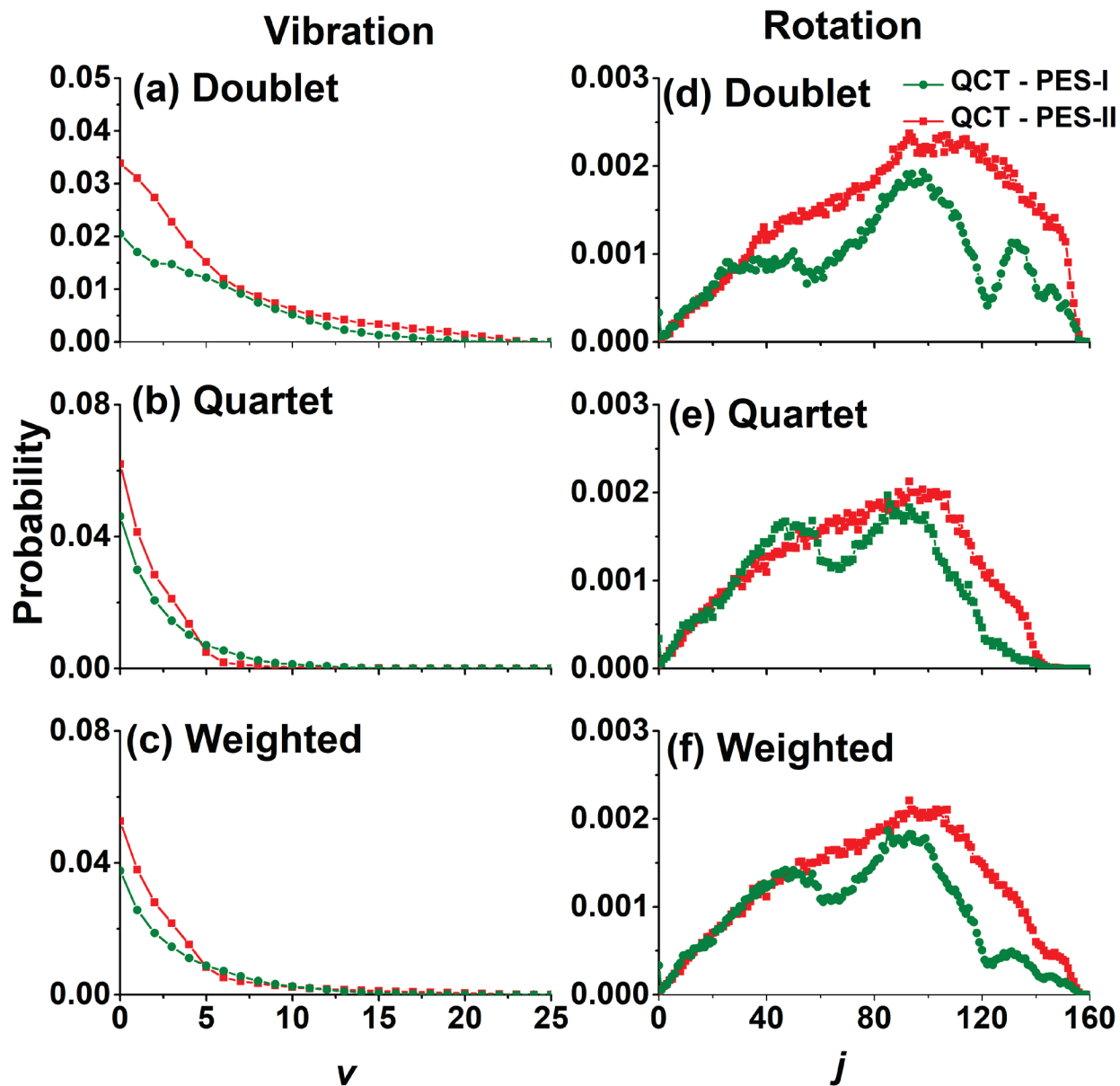
Figure 11. State-specific and weighted NO vibrational (left panels) and rotational (right panels) distributions calculated on PES-I (green) and PES-II (red).
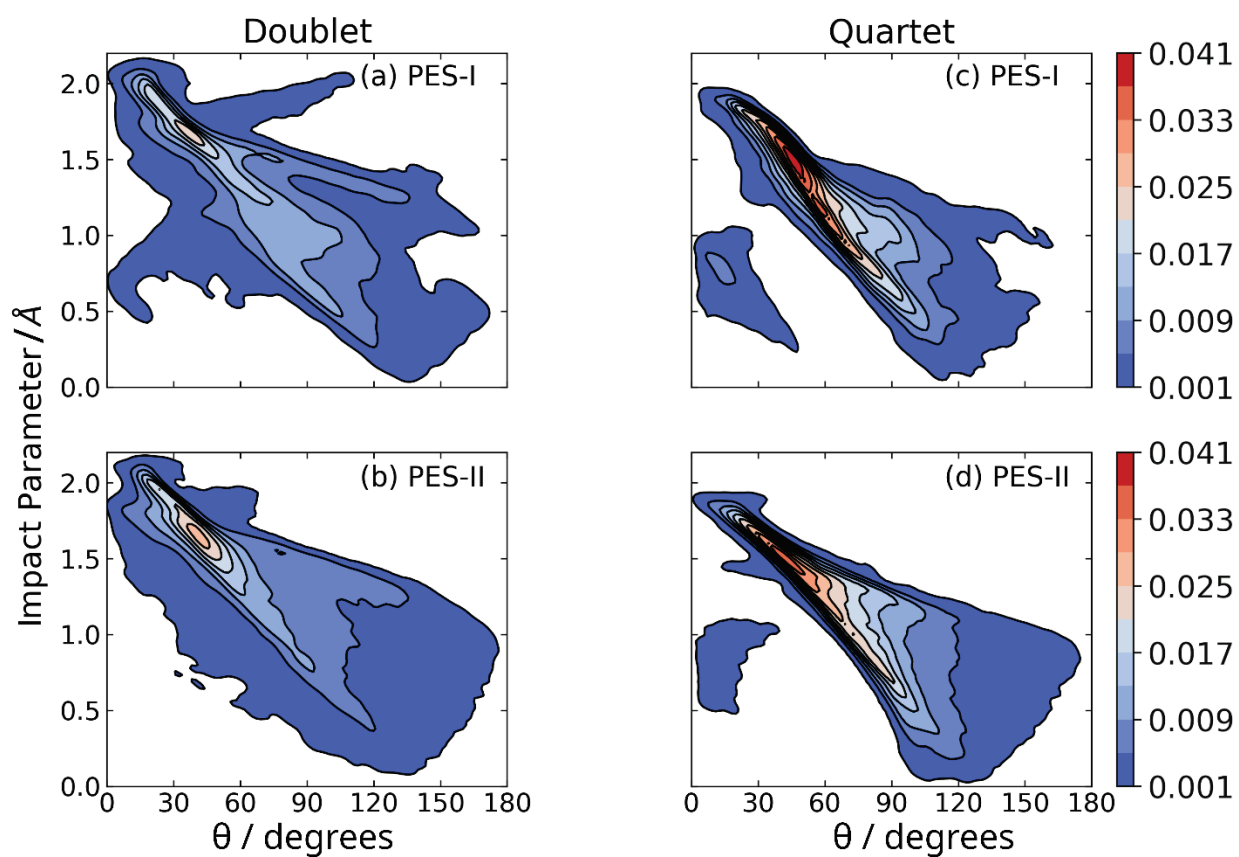
Figure 12. Correlation of the impact parameter and scattering angle for the reactive channel on both the doublet and quartet states of PES-I and PES-II.

TOC Graphic

$$^{14}N + {}^{16}O_2 \rightarrow$$

$^{16}O_2 + {}^{14}N$ 65% $^{16}O + {}^{14}N{}^{16}O$ 35%
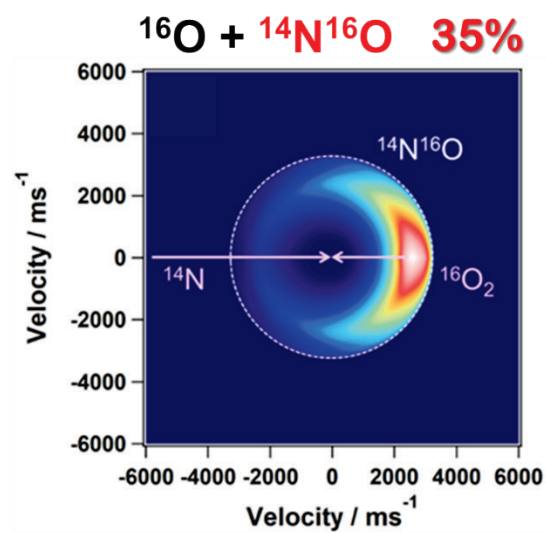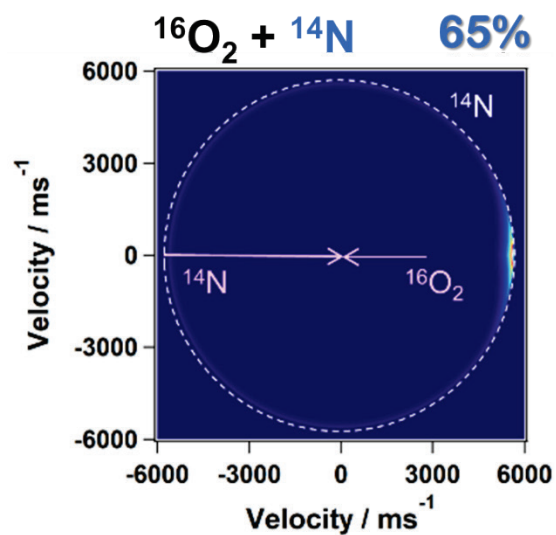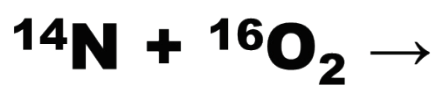
SUPPORTING INFORMATION

for

Experimental and Theoretical Studies of Hyperthermal N + O$_2$ Collisions

Adriana Caracciolo,[a] Juan Carlos San Vicente Veliz,[b] Dandan Lu,[c] Hua Guo,[c,*] Markus Meuwly,[b,*] and Timothy K. Minton[a,*]

[a] *Ann and H.J. Smead Department of Aerospace Engineering Sciences, University of Colorado Boulder, CO 80303, USA*

[b] *Department of Chemistry, University of Basel, CH-4056 Basel, Switzerland*

[c] *Department of Chemistry and Chemical Biology, University of New Mexico, Albuquerque, New Mexico 87131, USA*

*: corresponding authors: hguo@unm.edu; m.meuwly@unibas.ch; tminton@colorado.edu

Figure S1. (a) Experimental best-fit c.m. velocity-flux map for NO products using the c.m. distributions depicted in Figure 4c,d. (b) QCT-calculated c.m. velocity-flux map from PES-I. (c) QCT-calculated c.m. velocity-flux map from PES-II. In each panel, the arrows correspond to the initial velocity vectors of the reactants, and the radius of the dashed circle represents the maximum recoil velocity for the N-atom product, given the constraints of energy and momentum conservation. In each panel, the maximum flux has been normalized to a value of 1.0.
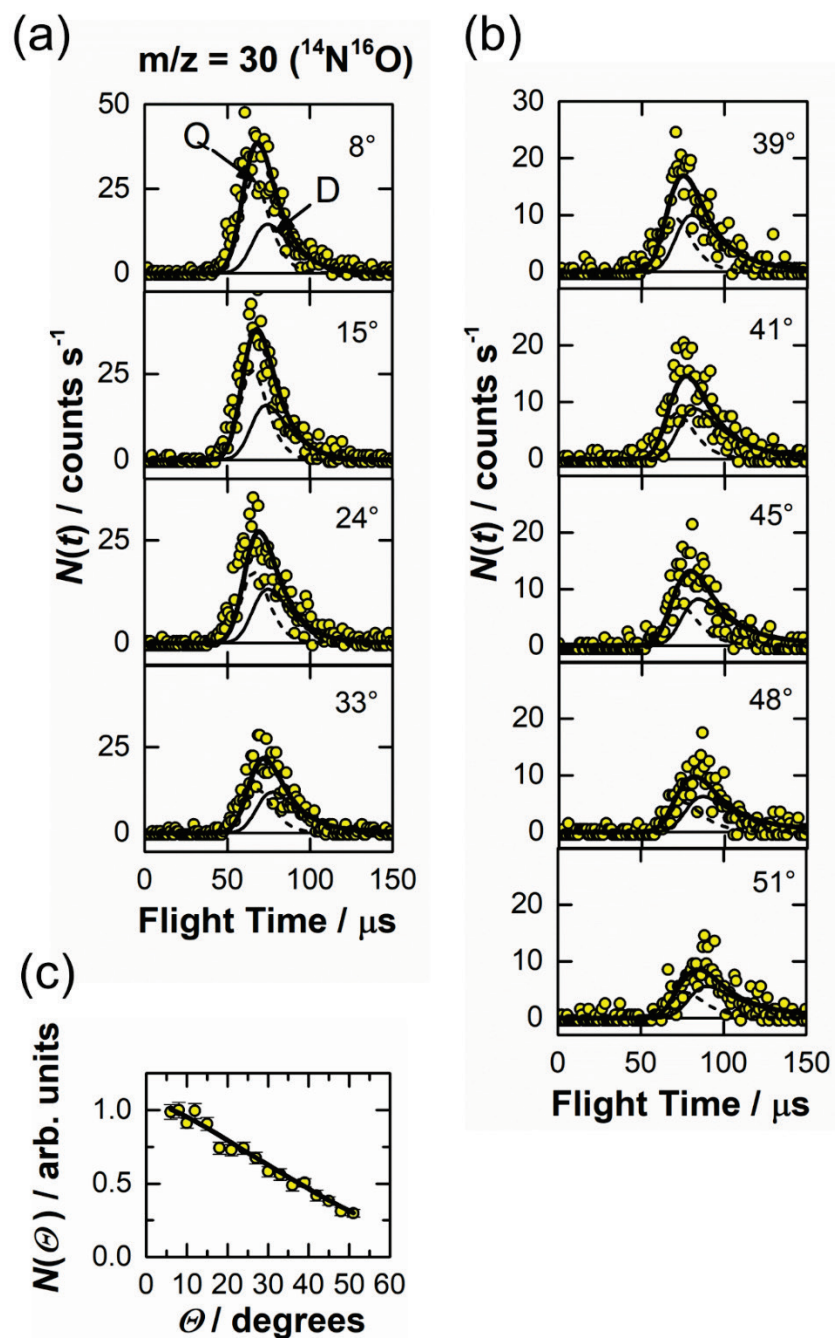
Figure S2. Representative TOF distributions in the forward (a) and sideways-backward (b) directions for the $^{14}N^{16}O$ products at $m/z = 30$ with $\langle E_{avl} \rangle = 109.5$ kcal mol^{-1}. (c) Laboratory angular distribution detected for the same m/z ratio. The black solid lines superimposing the raw data (yellow circles) represent the overall best-fit curve calculated from the forward convolution of the c.m. translational energy and angular distributions depicted Figure S3.

(a)

(b)
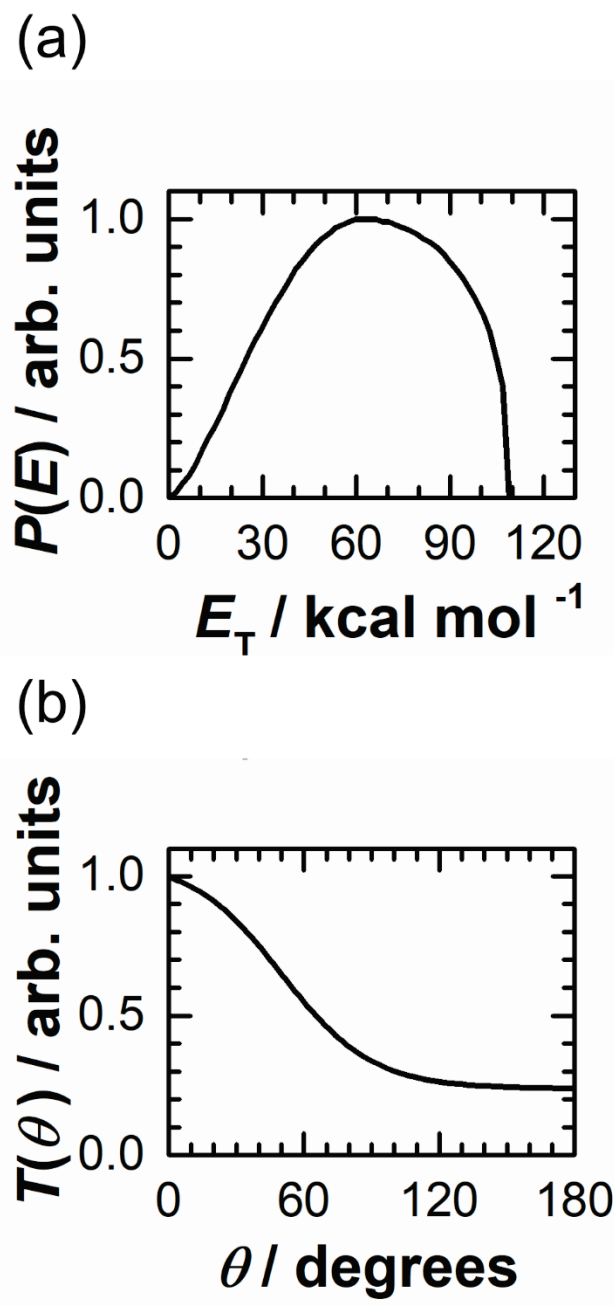
Figure S3. Best-fit c.m. translational energy (a) and angular (c) distributions (for the NO product) when only a single pair of these c.m. distributions is used.
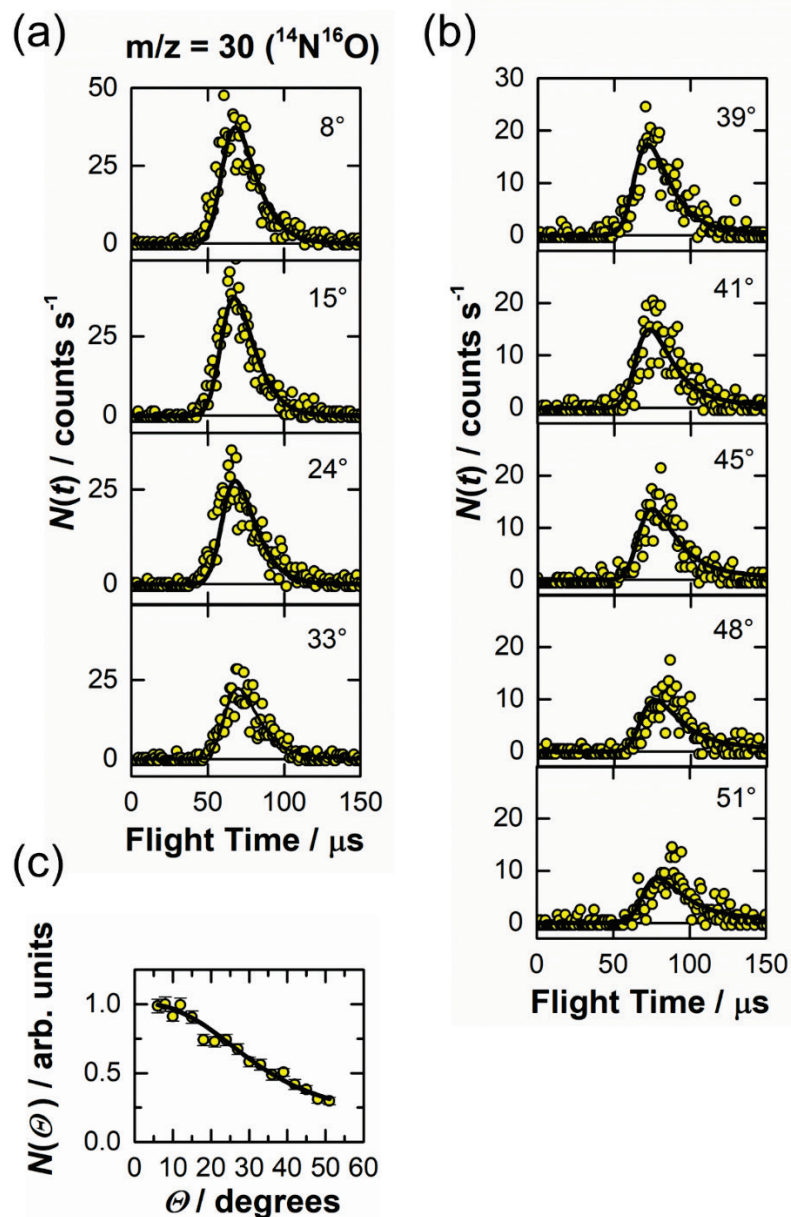
Figure S4. Representative TOF distributions collected in the forward (a) and sideways-backward (b) directions for NO products detected at $m/z = 30$ with $\langle E_{avl} \rangle = 109.5$ kcal mol^{-1}. The black solid lines superimposing the raw data (yellow circles) in (a) and (b) represent the overall best-fit curves calculated from the forward convolution of the c.m. translational energy and angular distributions depicted in Figure 6. The contributions of the two sets of c.m. distributions in Figure 6 to the TOF distributions are shown with their corresponding labels, D for the doublet (solid line) and Q for the quartet curve (dashed line).
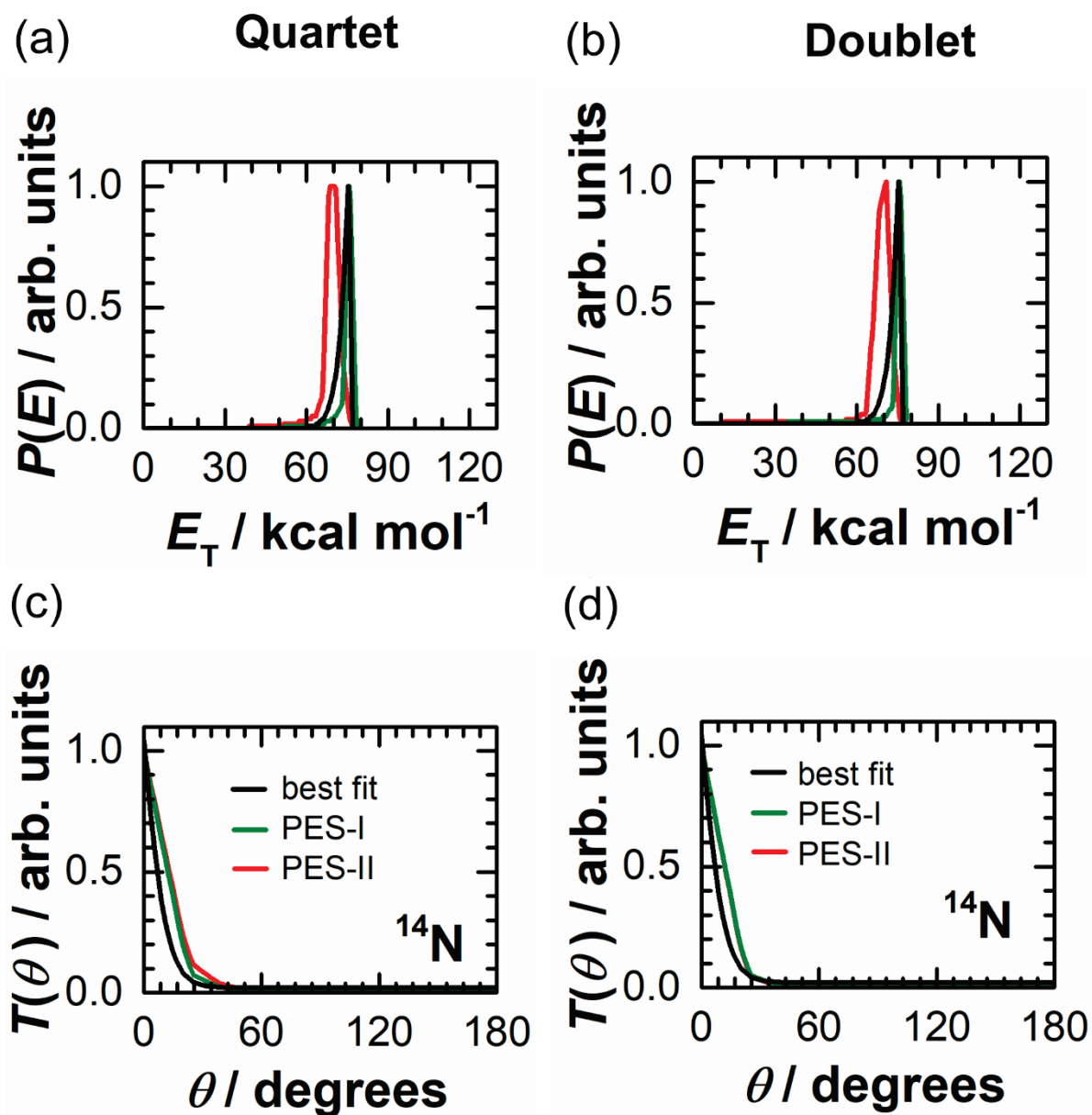
Figure S5. Best-fit c.m. (black) and QCT results from PES-I (green) and PES-II (red) for translational energy, (a) and (b), and angular, (c) and (d), distributions for N-atom products formed via the quartet (*lhs*) and doublet (*rhs*) surfaces.
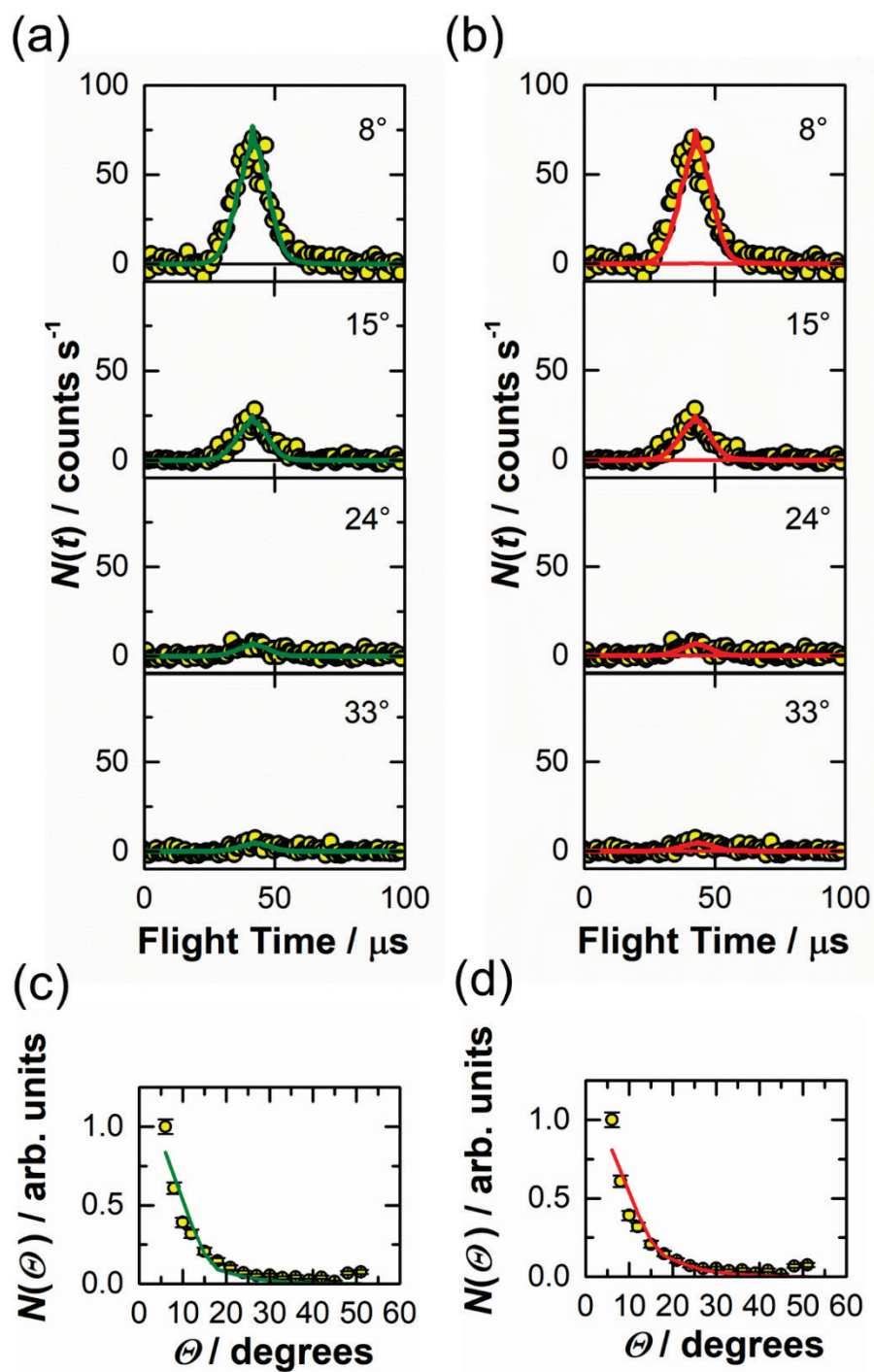
Figure S6. Experimental and predicted laboratory TOF (a,b) and angular (c,d) distributions for the N-atom product, with the predicted distributions from PES-I (green) and PES-II (red) superimposing the experimental data (yellow symbols). The predicted distributions were derived by the forward convolution of the corresponding c.m. translational energy and angular distributions in Figure 6.
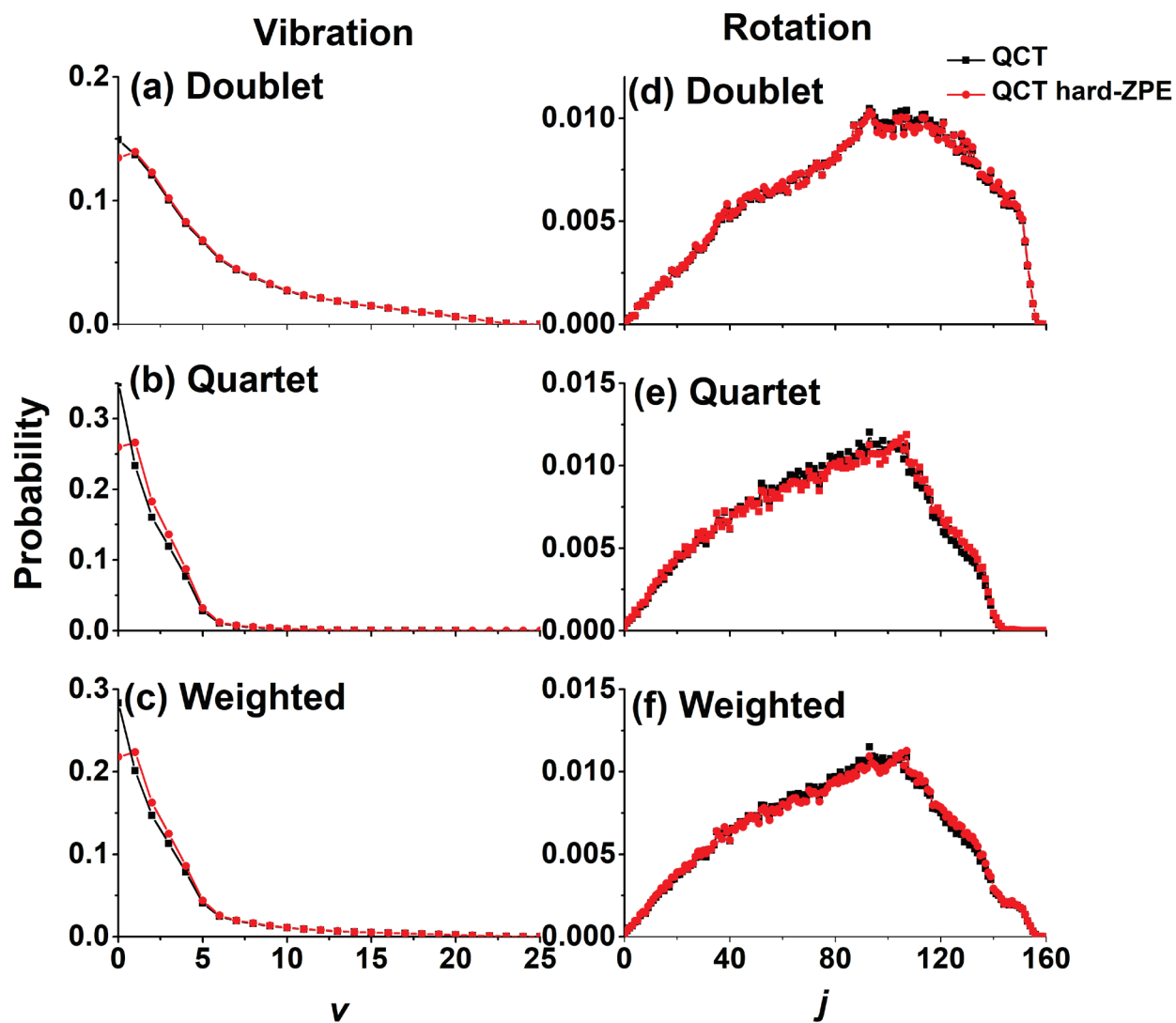
Figure S7. State-specific and weighted NO vibrational (left) and rotational (right) distributions calculated on PES-II, the red lines are the hard ZPE results.
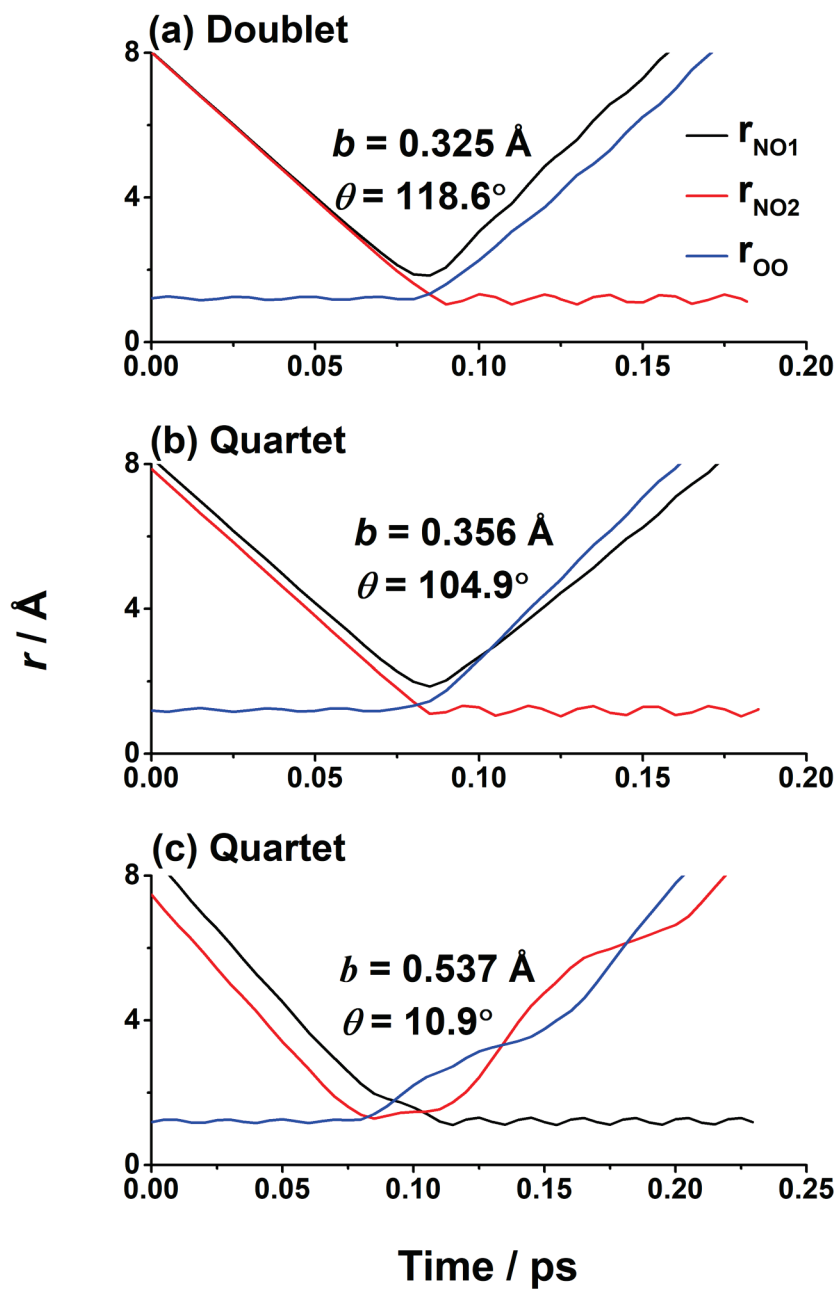
Figure S8. Variation of bond lengths with time for several trajectories. (a) Abstraction mechanism on doublet PES-II, (b) Abstraction mechanism on quartet PES-II, (c) Insertion mechanism on quartet PES-II.